Ti-substitution Facilitating Anionic Redox and Cycle Stability in P2-type $Na_{2/3}Mn_{2/3}Ni_{1/3}O_2$ Na-ion Battery Cathode

Neha Dagar[1], Samriddhi Saxena[1], Hari Narayanan Vasavan[1], Asish Kumar Das[1], Pratiksha Gami[1], Sonia Deswal[2], Pradeep Kumar[2], Karthik Chinnathambi[3], Vikram Rathee[4], and Sunil Kumar[1,*]

[1]*Department of Metallurgical Engineering and Materials Science, Indian Institute of Technology Indore, Simrol, 453552, India*

[2]*School of Physical Sciences, Indian Institute of Technology Mandi, Mandi, 175005, India*

[3]*Micron School of Materials Science and Engineering, Boise State University, Boise, ID 83725, USA*

[4]*Department of Physics and Astrophysics, Delhi University, Delhi, 110007, India*

*****sunil@iiti.ac.in

Abstract

P2-type layered oxides have attracted tremendous attention as the leading candidate for the cathode material in Na-ion batteries owing to their ease of synthesis and facile Na-ion diffusion. In this work, an in-depth investigation of the electrochemical behavior of P2-type (space group $P6_3/mmc$) 10% Ti-doped $Na_{2/3}Mn_{2/3}Ni_{1/3}O_2$ is carried out in different voltage ranges (1.5-4.0 V, 2.0-4.0 V, and 2.0-4.5 V). Ti^{4+} doping is found to disrupt the Na-ion/vacancy ordering and increase the Na-O2 layer spacings, which results in improved rate performance (~68 mAh g^{-1} at 5C in the 2.0-4.0 V range). In the 2.0-4.5 V range, $Na_{2/3}Mn_{0.567}Ti_{0.100}Ni_{1/3}O_2$ (NMNT) exhibits a reduced initial specific discharge capacity of 140 mAh g^{-1} and significantly improved capacity retention of 71% after 100 cycles due to enhanced reversibility of anionic redox. Better charge-discharge cycling stability of NMNT (80% capacity retention at 0.33C in 1.5-4.0 V range) evidences the Ti^{4+}-induced disruption of cooperative Jahn-Teller distortion. Galvanostatic intermittent titration results confirm higher Na^+ diffusion coefficients in NMNT. Interestingly, a marginally higher cathode-electrolyte interphase resistance in NMNT is endorsed by electrochemical impedance measurements, while the overall cell resistance and the charge-transfer resistance are much lower (by ~45% and ~56.7%, respectively) than in $Na_{2/3}Mn_{2/3}Ni_{1/3}O_2$.

Keywords: Sodium-ion batteries; Layered oxides; Anionic redox; Cycle stability

1. Introduction

Cheaper and sustainable electrochemical energy storage systems are one of the key requirements for the adoption of renewable but intermittent energy sources for large-scale electric grid and electric vehicles (EVs) applications.[1-2] While lithium-ion batteries (LIBs) have been widely used in portable electronic devices and EVs due to their superior energy density and excellent cycling performance, serious concerns remain regarding the limited reserves and cost associated with lithium supply.[2-3] High-performance Na-ion batteries (NIBs) are realistic alternatives for LIBs due to similarities in operation and the abundance of raw materials for sodium precursors.[4-5] Moreover, there have been tremendous improvements in the specific capacity and rate performance of Na-ion batteries in recent years, and Na-ion cells with energy density matching that of $LiFePO_4$-based LIBs have been developed.[2, 6-7] Accordingly, major manufacturers have announced the commercial-scale production of Na-ion batteries, and their use in electric vehicles has also been demonstrated. [7-9]

The choice of cathode material plays a significant role in determining the energy density, cyclability, and rate performance of NIBs. Accordingly, various compound families, including layered oxides, polyanionic, Prussian blue analogs, etc., have been extensively investigated.[4-5, 10-12] Among various candidates, Na-ion layered transition metal oxides (Na_xTMO_2 with $0 < x \leq 1$ and TM is a redox-active element(s), such as Mn, Ni, Co, Fe, Cr, Cu, V, or a combination of these) are considered front-runners for application as the cathode in NIBs due to their easier and scalable synthesis process, high reversible capacity, flexibility in accommodating different cations, and phase tunability.[13-26] Layered oxides are classified according to the coordination geometry of the sodium site (prismatic P or octahedral O) and the number of TM-O2 layers in one crystallographic unit cell.[27] While O3 structures are desirable for their high specific capacity, P2-type phases (usually with low Na content <0.8) offer fast Na-ion transport owing to the low diffusion barrier between adjacent prismatic sites in the Na-O2 layers.[5, 28] There has been a recent focus on stabilizing P-type phases with high Na content to achieve high specific capacity and good rate performance simultaneously.[29-31]

P2-type $Na_{2/3}Mn_{2/3}Ni_{1/3}O_2$ (NMN), first reported by Dahn's group, has attracted considerable attention due to its electrochemical performance.[19, 32] NMN delivers a reversible capacity of ~161 mAh g^{-1} when cycled in 2.0−4.5 V at a low C-rate, suggesting that almost all Na-ion can be (de)intercalated from the structure. However, this capacity is accompanied by an irreversible P2-to-O2 type phase transition due to electrostatic repulsion induced gliding of oxygen layers when the amount of Na in NMN falls below 1/3 at high charging voltage. The severe volume change (~22%) during this phase transformation is detrimental to the long-term cycle stability of NMN.[32-34] The cyclability of NMN is improved when the upper cut-off voltage is reduced to 4 V; however, this is at the expense of reduced specific capacity.

The structural degradation and resultant capacity loss (upon cycling) in NMN are also caused by Na^+/vacancy ordering at intermediate Na stoichiometry and Jahn-Teller distortion due to the activation of Mn^{3+} upon discharging the cathode to voltages below 2 V.[34-36] The oxygen evolution in Mn-based layered oxides is believed to arise from the weaker Mn-O bond. Several substitutions of Mn^{4+} and Ni^{2+} in NMN have been adopted to improve the structure stability by suppressing the severity of P2-O2 phase transformation when charged to voltages exceeding 4 V.[22, 28, 34, 37-39] Doping of different pillar-ions is also known to suppress the cooperative Jahn-Teller distortion in Mn-based layered oxides [36]. Ti-Mg co-doping in $Na_{0.67}Fe_{0.4}Mn_{0.6}O_2$ was reported to enhance the cationic/anionic redox reaction reversibility attributed to the stabilized surface and bulk structure at high voltages with an excellent capacity of ≈ 210 mAh g^{-1} at 20 mA g^{-1}.[40] Ti-doped $Na_{2/3}Mn_{1/2}Ni_{1/3}Ti_{1/6}O_2$, first reported by Yoshida et al., showed improved cyclablity via reduced volume changes upon Na de-intercalation/intercalation.[22] 10% Mg/Sc substitution for Ni^{2+} in NMN was found to suppress the oxygen redox, resulting in improved cycling stability. Interestingly, the Mg-doped cathode showed much better cycling stability than the Sc-doped sample despite having a larger volume change during sodiation. [33] Another important study demonstrated a reversible capacity of ~88 mAh/g with solid-solution reaction-type sloping discharge curves when cycled between 2.5 V and 4.15 V. [41] A high specific capacity of ~220 mAh g^{-1} and improved cycling stability were achieved in Ti-substituted $Na_{2/3}Li_{2/9}Mn_{7/9}O_2$, which was attributed to synergistic contributions from both Mn-redox and O-redox processes. [42]

In this work, an in-depth investigation of the electrochemical behavior of 10% Ti-doped $Na_{2/3}Mn_{2/3}Ni_{1/3}O_2$ is carried out by cycling this cathode in different voltage ranges (1.5-4.0 V, 2.0-4.0 V, and 2.0-4.5 V) to study the impacts of Ti^{4+} on the reversibility of anionic redox, Na-ion vacancy ordering, and suppression of cooperative Jahn-Teller distortion. 10% Ti was chosen as the optimal doping in view of the literature and the fact that higher Ti doping was found to decrease the specific capacity and electronic conductivity.[33, 43-46] $Na_{0.667}Mn_{0.567}Ti_{0.100}Ni_{0.333}O_2$ (NMNT) exhibited a slightly reduced initial specific capacity of 140 mAh g^{-1} at 13 mA g^{-1} and improved capacity retention of 71% after 100 cycles when cycled in 2.0-4.5 V range. Ti-doping improved the Na^+ diffusion by increasing the Na-O2 interlayer spacing, which resulted in improved rate performance. Further, the NMNT sample delivered enhanced anionic redox activity and a higher average discharge voltage even when cycled in 2.0-4.0 V.

2. Experimental Section

2.1. Synthesis of NMN and NMNT

The $Na_{2/3}Mn_{2/3}Ni_{1/3}O_2$ (NMN) and $Na_{2/3}Mn_{0.567}Ti_{0.10}Ni_{1/3}O_2$ (NMNT) powders were synthesized via the conventional sol-gel method using the stoichiometric ratio of Na_2CO_3 (sodium carbonate), $C_4H_6MnO_4\cdot 4H_2O$ (manganese acetate tetrahydrate), $C_4H_6NiO_4\cdot 4H_2O$ (nickel acetate tetrahydrate), and $CH_3CH(O\text{-})CO_2NH_4]_2Ti(OH)_2$ (Titanium(IV) bis(ammonium lactato)dihydroxide) as precursors which were dissolved in deionized water (DI). The solutions were kept for stirring for homogeneous mixing. Ethylene glycol and citric acid were added (molar ratio1:2) to the solutions to form a gel, followed by drying the gel by heating it at 120 °C. The denitrification and decarbonization were done by heating the resultant powders at 650 °C for 12 h. Finally, the powders were calcined at 900 °C for 12 h to obtain the desired phase. The prepared samples were stored in an argon atmosphere glove box (MBraun EasyLab Pro, H_2O & O_2 <0.1 ppm).

2.2. Characterizations

For the phase confirmation, powder x-ray diffraction (XRD) was performed on the NMN and NMNT samples using an Empyrean diffractometer from Malvern Panalytical (Cu-K_α radiation wavelength $\lambda \approx 1.54$ Å) in the 2θ range of 10° to 70°. The morphology and elemental mappings of the synthesized powders were studied using a scanning electron microscope (FESEM model JEOL-7610). For the x-ray photoelectron spectra (XPS), a Thermofisher Scientific Naxsa instrument with a 1486.6 eV Al-Kα x-ray source was employed to confirm the oxidation states of various constituents of NMN and NMNT. A JEOL-2100 TEM was used for transmission electron microscopy (TEM) studies and samples for these were prepared by drop-casting the powder on the carbon-coated Cu grids.

2.3. Electrochemical measurements

The cathode slurry was prepared using NMP (N-Methyl-2-Pyrrolidone) as the solvent, PVDF (Polyvinylidene fluoride) as the binder, Ketjen Black as the conducting carbon, and NMN/NMNT powders, respectively, as the active material. The ratio of PVDF, Ketjen Black, and active material in both slurries was 15:10:75. The mixture was stirred for 10 h to form a uniform slurry. The slurry was then coated on aluminum foil (current collector) using an automatic film coater and a doctor's blade. Subsequently, the coated cathode slurry was dried in a vacuum oven overnight. The coated cathodes were then punched into 14 mm diameter discs. For the electrochemical testing, CR2032 coin cells employing these cathodes were fabricated using sodium metal as the anode and glass fiber (Whatman G/D) as the separator. 1M $NaClO_4$ in a 1:1 solution of EC:PC (ethylene carbonate and polypropylene carbonate) was used as the electrolyte. The mass loading for the active material was ~3–4 mg cm^{-2} for both samples. The prepared coin cells were investigated for cyclic voltammetry (CV) using a Keithley Source Meter (Model 2450 EC). The galvanostatic intermittent titration technique (GITT) at 0.1C and galvanostatic charge-discharge (GCD) behaviors at various C-rates (1C = 130 mA g^{-1}) were studied using a Neware battery tester, model CT-4008. Further, the performance of both cells was compared. An NF Corp LCR meter (model: ZM 2376) was used to obtain the impedance data at room temperature in the 10 mHz–1 MHz frequency range.

3. Results and Discussion

3.1. Crystal structure

The crystalline phase of NMN and NMNT calcined at 900 °C was confirmed with the help of XRD studies. The room temperature XRD patterns of both these samples are shown in Fig. 1(a). All major peaks in the patterns match with those of the P2 phases reported in the literature. [18-19, 32, 34, 47] Minor impurity peaks (at ~37° and 43°) belonging to NiO were also observed in both samples, and the intensity of these peaks seems to be lesser in the XRD pattern of the NMNT sample. [48] The presence of the NiO impurity phase could be attributed to the Na volatilization, a limited solubility of Ni^{2+} in the lattice, and chemical inhomogeneities during calcination. [49-50] A magnified view of the XRD patterns in the 25°-30° range (Fig. 1(a) inset) shows Na^+/vacancy ordering peaks in NMN. [41] The absence of these ordering peaks in the pattern of the NMNT sample confirms that Ti doping effectively suppresses the Na^+/vacancy ordering. A slight shift in the XRD peak positions towards lower angles is also noticeable with Ti doping. This suggests that Ti doping increases the volume of the unit cell.

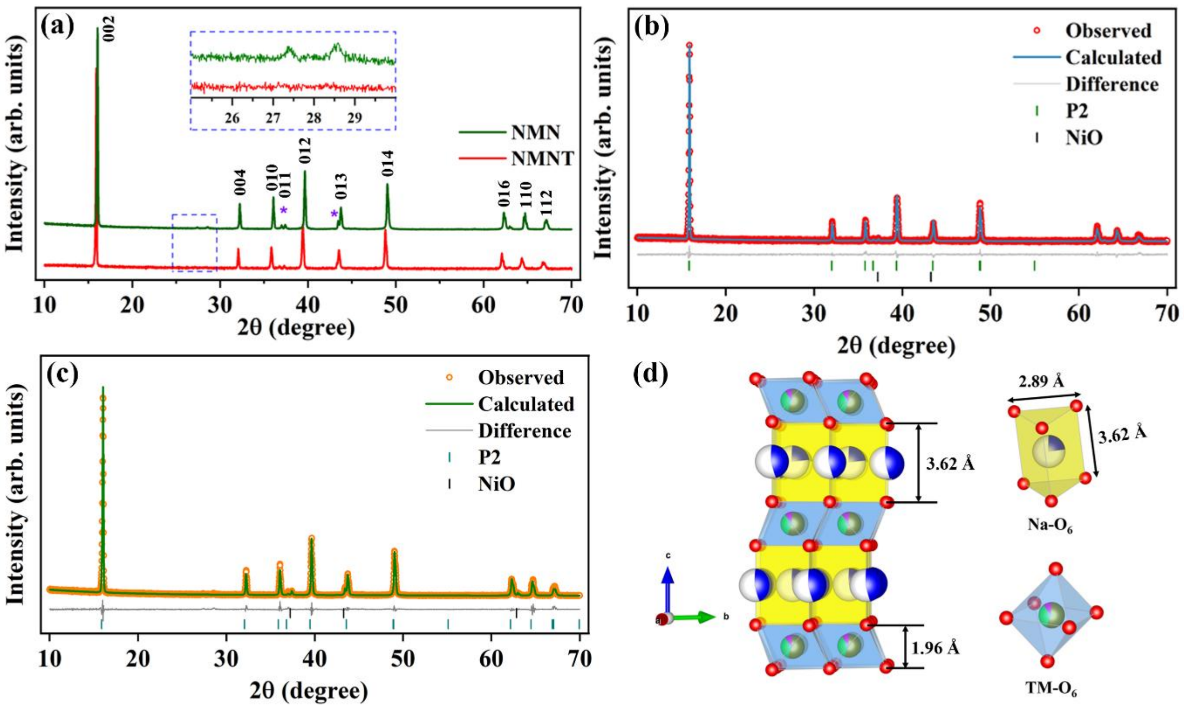

Figure 1: (a) XRD patterns for NMN and NMNT. The star symbols (*) indicate NiO peaks, and a magnified view of patterns in the 25-30° range demonstrates the absence of the Na$^+$/vacancy ordering peaks in NMNT. Rietveld refinement profiles for NMNT powder (b) and NMN powder (c). (d) Schematic of NMNT crystal structure.

To quantify these results, Rietveld refinement of powder XRD data was done using the *TOPAS academic* software, and the results are shown in Fig. 1(b) and 1(c) for NMNT and NMN, respectively.[51] A good match (goodness of fit =1.24 for NMNT and 1.62 for NMN) between the observed and the calculated patterns suggests that there are no other impurity peaks apart from the intended P2-phase (space group $P6_3/mmc$) and minor NiO (space group $Fm\bar{3}m$). The phase fraction of NiO decreased from ~2% for NMN sample to ~1% for NMNT. This suggests that Ti doping in NMN suppresses not just the Na$^+$/vacancy ordering but also the formation of the NiO impurity phase. The calculated lattice parameters and other crystallographic parameters are shown in Table 1. Both lattice parameters (*a* and *c*) were larger in the Ti-substituted sample (NMNT) than in NMN. Accordingly, unit cell volume also increases from 80.56 Å^3 for the NMN sample to 81.20 Å^3 for the Ti-doped sample. This increase in lattice parameters confirms the successful incorporation of Ti in NMN crystal structure as the substitution of Mn^{4+} (ionic radius in 6 coordination = 0.53 Å) by larger Ti^{4+} (ionic radius in 6 coordination = 0.605 Å) is expected to expand the lattice.[52]

P2 materials are well known for facile Na^+ diffusion because of the prismatic environment of Na. To check the impact of increased lattice parameters on the bottleneck area of NMNT for Na-ion diffusion, Na-O2 interlayer spacing was calculated for both NMN and NMNT samples. For P2-type materials, the Na-O2 interlayer spacing ($S_{\text{Na-O2}}$) is given by the formula:

$$S_{\text{Na-O2}} = c[0.5 - 2O_z] \quad (1)$$

$$S_{\text{TM-O2}} = 0.5c - S_{\text{Na-O2}} \quad (2)$$

where c is the lattice parameter of the P2-type unit cell and O_z is the fractional coordinate of oxygen ion along the z-axis. A schematic of the crystal structure of NMNT is shown in Fig. 1(d). The values of O_z for both the samples calculated from the Rietveld refinement of XRD data are given in Tables S1 and S2 (Supporting Information). The value of $S_{Na\text{-}O2}$ increases from 3.50 Å for NMN to 3.62 Å for NMNT, accompanied by a contraction of TM-O2 layer spacing ($S_{\text{TM-O2}}$) from 2.07 Å to 1.96 Å. Similar results concerning the expansion of Na-O2 layer spacing and contraction of TM-O2 layer spacing upon Ti doping are reported in the literature for other layered oxides.[49, 53-54] This contraction is due to the stronger Ti-O bond as compared to the Mn-O bond.[49, 52] Consequently, the Na-ion diffusion bottleneck area increased to 10.46 Å^2 for the Ti^{4+}-substituted sample from 10.07 Å^2 for pure NMN. The enlarged area reduces the barrier for Na^+ diffusion. This is also confirmed by the values of the diffusion coefficient in GITT (discussed in the later section). To check the chemical stability of NMNT, the XRD measurement was carried out after exposing the powder sample to an ambient atmosphere for 30 days, and no changes in the XRD pattern (in terms of the appearance of impurity phases or changes in the FWHM or peak positions, Fig. S1) were observed, indicating the air-stability of NMNT. No peak corresponding to the O-H bond is observed in the FTIR spectrum for the NMNT sample exposed to ambient air (Fig. S2) and the spectrum matches with that of pristine NMNT sample, further confirming the air stability of this sample.

Table 1: Refined structural parameters for $Na_{2/3}Mn_{2/3}Ni_{1/3}O_2$ (NMN) and $Na_{2/3}Mn_{0.567}Ti_{0.10}Ni_{1/3}O_2$ (NMNT) powders calcined at 900 °C.

Sample	NMN	NMNT
Crystal system	Hexagonal	
Space group	$P6_3/mmc$	
Cell Parameters, Å		
	a = 2.8873(5)	a = 2.8966(4)
	c = 11.158(3)	c = 11.175(3)
Cell Volume V, Å^3	80.56(3)	81.20(3)
Z	2	2
Phase density (g/cm^3)	~ 4.27	~ 4.20

3.2. Microstructure

The morphologies of the NMN and NMNT powder samples obtained by FESEM are shown in Fig. 2(a) and 2(b), respectively. Both samples show hexagonal-shaped particles, and the particles seem to be agglomerated. Further, in NMNT, the particles appear smaller and have a lower aspect ratio than those of NMN. The average particle size calculated using the *ImageJ* software was found to be 1.9 ± 0.4 μm (standard deviation) for NMNT and 2.5 ± 0.4 μm for NMN [55]. The equilibrium shape of a crystal is determined by the relative surface energies of various surfaces. {001} surfaces are known to be more stable as compared to {100} & $\{\bar{1}10\}$ surfaces in layered oxides, resulting in a thin hexagonal-type plate morphology. Ti doping changes the energies of various NMN surfaces, which increases the area of lateral surfaces relative to basal surfaces.[45] Such modification in the microstructure is helpful in improving the rate performance of P2-type materials as the Na-ion diffusion in these materials is across the lateral planes.

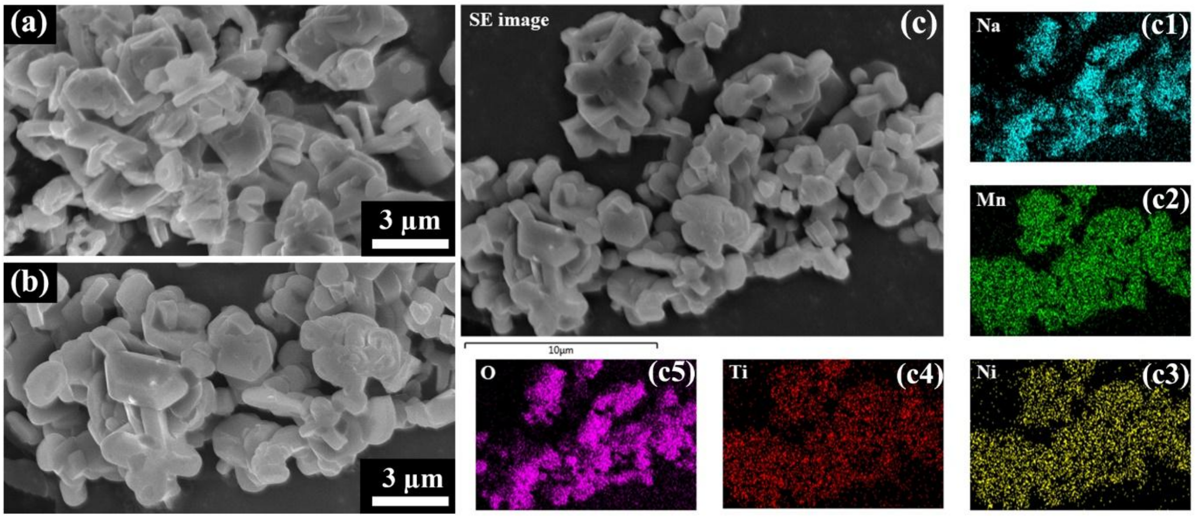

Figure 2: SEM images of (a) NMN and (b) NMNT powder samples. (c) Secondary electron (SE) image and EDS elemental mappings (c1-c5) of NMNT powder sample.

Energy dispersive X-ray spectroscopy (EDS) was performed for elemental characterization and elemental mappings of NMNT and NMN, as depicted in Fig. 2(c1-c5) and Fig. S3, respectively. No segregation of constituent elements is apparent in either of the samples. Additionally, Table S3 provides the atomic % of the various constituent elements of NMN and NMNT samples, which are in close agreement with the values expected from the nominal compositions.

To further examine the local structure of the NMNT sample, TEM was employed, and the obtained bright field image, high resolution (HRTEM), and selected area diffraction pattern are shown in Fig. 3. The lattice fringes in Fig. 3(b) have an interlayer spacing of ~2.5 Å which corresponds to the (100) planes of P2 phase and is consistent with the XRD refinement results. The SAED pattern (Fig. 3(c)) recorded along [001] zone-axis shows the hexagonally arranged diffraction spots that well matched with the (100), (010), $(\bar{1}10)$, $(\bar{1}00)$, $(0\bar{1}0)$, and $(1\bar{1}0)$ planes of NMNT. Faint superlattice diffraction spots (white circles) confirm the Mn-Ni honeycomb ordering with ($\sqrt{3} \times \sqrt{3}$)-R30° superstructure. [56]

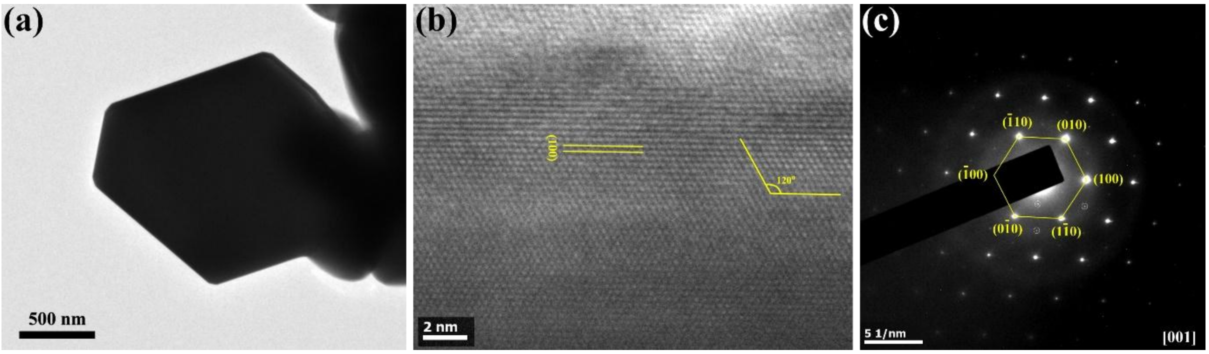

Figure 3: (a) Bright-field and (b) HRTEM image of NMNT sample. (c) The SAED pattern recorded along the [001] zone axis. The weak superlattice reflections are indicated by white circles.

3.3. X-ray photoelectron spectroscopy

X-ray photoelectron spectroscopy (XPS) measurements were used to ascertain the compositions and ion valencies. Figures 4 and S4 depict the XPS spectra of Mn 2p, Ni 2p, Na 1s, and Ti 2p for NMN and NMNT samples. Mn 2p spectra (Fig. 4(a)) show 2 peaks located at the binding energies of ~641.5 and ~653.0 eV that correspond to Mn 2p$_{3/2}$ and Mn 2p$_{1/2}$, confirming the existence of Mn in a 4+ oxidation state in both samples. Another broad hump at ~645 eV is observed in Mn 2p spectra. A similar feature in Mn 2p spectra is also observed in other reports. [57-58] The Ni 2p spectra (Fig. 4(b)) display two characteristic sharp peaks attributed to Ni 2p$_{3/2}$ (at the binding energy of ~854.5 eV) and Ni $2p_{1/2}$ (at ~872.2 eV). The other two broader peaks in spectra are the Ni 2p satellite peaks. Similar to Mn, no difference in the valence states of Ni is apparent from the Ni 2p spectra, and Ni-ions maintain a 2+ oxidation state in pristine NMN and NMNT samples. Ti $2p_{3/2}$ (at ~457.3 eV) and Ti $2p_{1/2}$ (at ~463.1 eV) peaks with a splitting of ~5.8 eV (Fig. S4) suggest the presence of Ti^{4+} in NMNT. The Na 1s spectra for NMN and NMNT, given in Fig. S4, show a peak at ~1070.6 eV, which is consistent with the Na^{+}. No change in peak position is noticeable; however, a slight asymmetry in the peak is noteworthy and could be due to the distinct edge-shared (Na_e) and face-shared (Na_f) environments of Na-ions in the P2-type structure.[59]

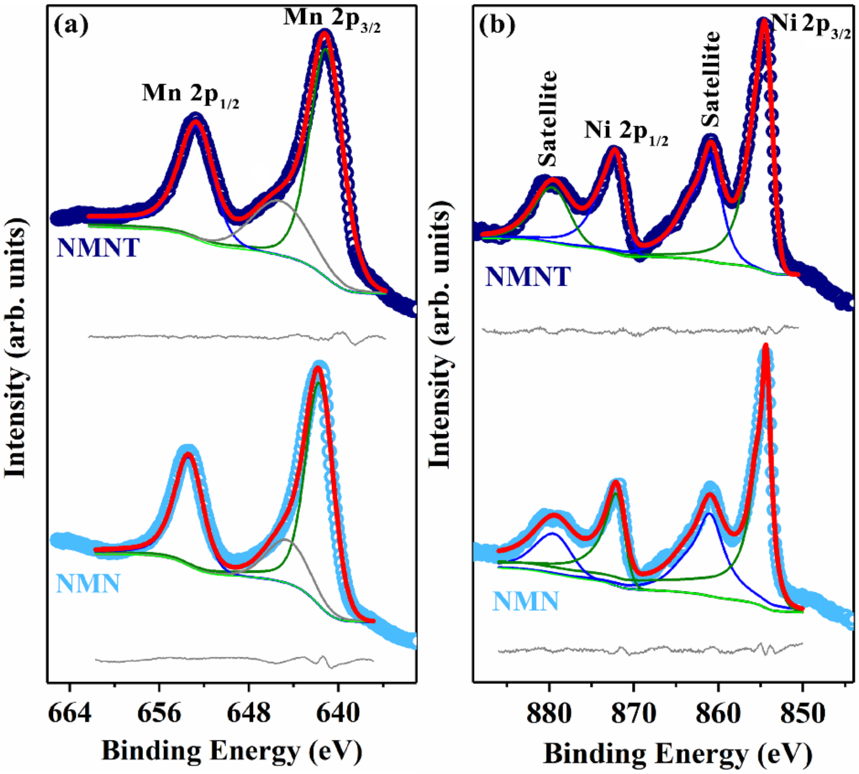

Figure 4: Experimental and fitted XPS data for (a) Mn 2p and (b) Ni 2p for NMN and NMNT samples. Gray lines at the bottom show the fitting residual curves.

3.4. Cyclic voltammetry

The redox activity of the NMN and NMNT electrodes was confirmed by cyclic voltammetry (CV) in the 2.0-4.0 V range at a scan rate of 0.1 mV/s, as shown for the first three cycles in Fig. 5. Figure 5(a) shows three prominent features present at ~3.17/2.91 V, ~3.50/3.17 V, and ~4.00/3.57 V for NMN. These features at ~3.17/2.91 V and ~3.50/3.17 V are attributed to the $Ni^{2+/3+/4+}$ redox activity.[23, 60] The incomplete oxidation peak at 4.0 V corresponds to the oxygen ($O^{2-/n-}$) redox.[58] On the other hand, in the Ti-doped sample, only two broad features are observed during an increase in voltage from 2.0 V to 4.0 V, and both are reversible.

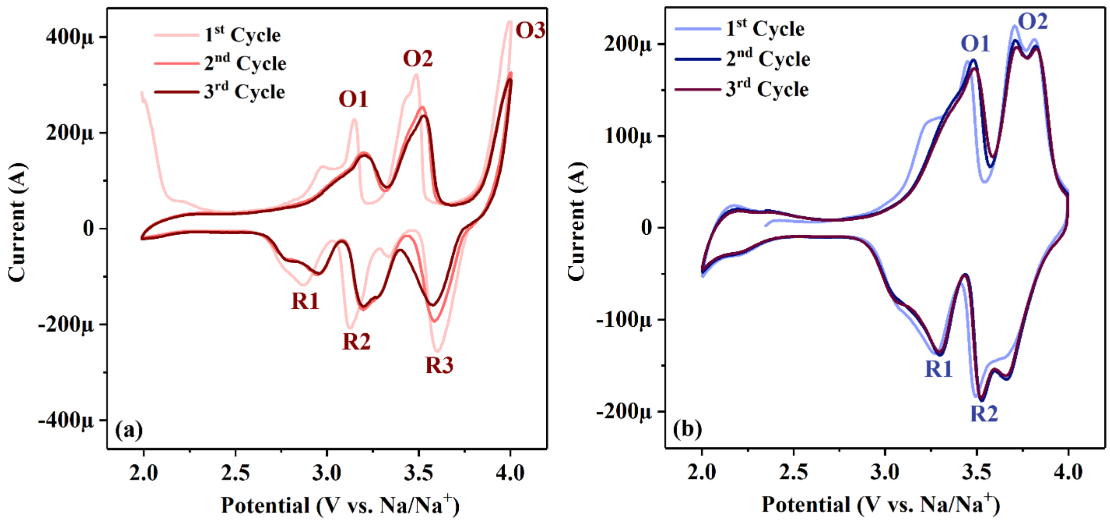

Figure 5: CV curves at a scan rate of 0.1 mV s^{-1} of (a) NMN and (b) NMNT.

There is a change in the peak currents and peak positions in CV curves for both samples after the first cycle, which can be attributed to the irreversible changes in the electrodes and the formation of passivation layers. A good overlapping of the 2nd and 3rd cycles CV curves demonstrates their excellent electrochemical reversibility. The third feature (O3/R3 at 4.00 V/3.75 V in NMN) is not observed in the CV of NMNT (Fig. 5(b)). Interestingly, the peak R1 shifts from 2.91 V (in 2nd cycle) to 3.34 V on Ti-doping in NMN. A similar increase in R2 peak potential is also observed. Further discussion on the shift in the redox peaks is provided in the differential capacity (dQ/dV) vs. voltage (V) plots. Hence, Ti-doping not only shifts Ni-redox to a higher voltage but also shifts the anionic redox activity above 4 V.

3.5. Galvanostatic charge-discharge

To further probe the impact of Ti substitution on the electrochemical behavior of NMN, galvanostatic charge-discharge (GCD) measurements were conducted on half-cells employing NMN and NMNT as cathodes. The voltage ranges of 1.5-4.0 V, 2.0-4.0 V, and 2.0-4.5 V were selected to examine the cationic and anionic redox activities. Figure 6(a) represents the voltage profiles for NMN and NMNT samples in the 2.0-4.0 V range at 0.1C. The discharge specific capacities are found to be similar, ~91 mAh g^{-1} for NMN and ~90 mAh g^{-1} for NMNT. However, the initial Coulombic efficiency of the NMNT sample is significantly higher (~94.2%) than that of NMN, which is only ~81.3%.

Multiple voltage plateaus corresponding to various phase transitions and Na-ion/vacancy ordering are visible in the charge-discharge profile of NMN. [35] It is observed that the Ti doping shifts charge and discharge plateaus to higher voltages. The voltage plateau for a given cathode depends on the nature of the redox activity, crystal structure, and local electronic structure. The shift in voltage plateaus to higher potentials (Fig. 6(a)) is due to the changes in the environment and bonding of Na-ions resulting from the modification of the TM-O2 layer. It is important to note that Na-ions share an edge and a face of the prism with the transition metal octahedra in NMN. Any modification in the TM-O2 layer is bound to affect the Na-ions (de)intercalation behavior. Ti doping not only increased the overall volume of the unit cell, but the Ti-O bond is also stronger than the Mn-O bond.

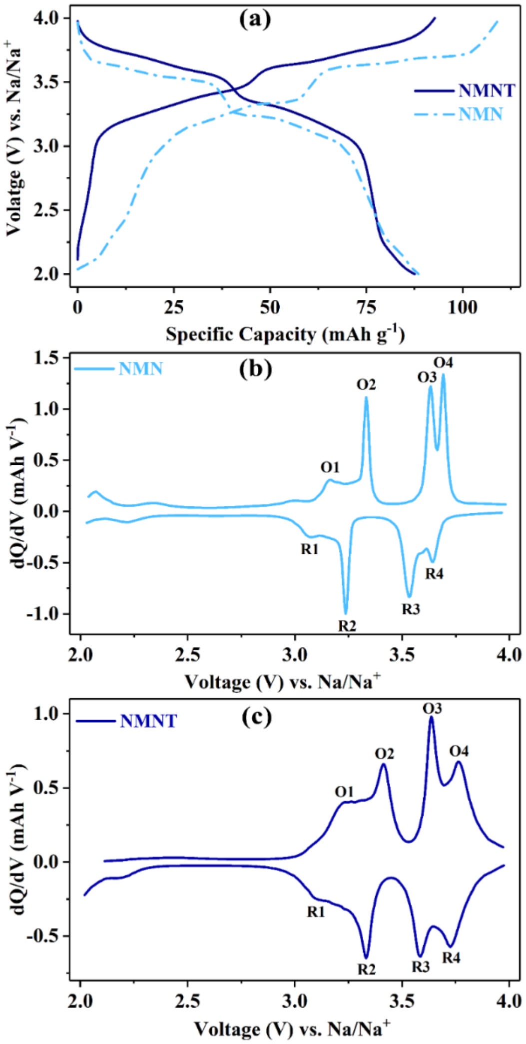

Figure 6: (a) First cycle GCD curves of NMN and NMNT at 0.1 C. Corresponding dQ/dV vs. V plots for (b) NMN and (c) NMNT.

Another noticeable feature in Fig. 6(a) is the absence of small plateaus in the 2.0-2.5 V range in the GCD curve of NMNT. These plateaus are known to arise from the Na^+/vacancy ordering, suggesting the disruption of this ordering in NMNT.[34-35] This result is in line with the observation from the XRD analysis. The differential capacity (dQ/dV) vs. voltage (V) plots for NMN and NMNT are shown in Figs. 6(b) and 6(c), respectively. The multiple peaks observed are attributed to Ni redox activity. The peaks in the dQ/dV versus V plot for the NMNT sample are broader than in NMN. This could be due to Ti^{4+}-induced structural disorder, suppressing the sudden phase transformation responsible for step-like features in the GCD profile. Further, a shift in peak positions towards higher voltage is also noticed upon Ti doping in the NMN sample. O2/R2 redox peaks shift from 3.33/3.23 V for NMN to 3.42/3.33 V for NMNT. A similar change in other peaks is also observed. Interestingly, the polarization for O2/R2 and O3/R3 peaks decreases from 0.1 V (for NMN) to 0.08 and 0.05 V (for NMNT), respectively. This is attributed to the lower charge-transfer resistance in NMNT, as discussed later in the EIS section. It is to be noted that the NMN cathode, prepared in this work, shows ~ 25 mAh/g capacity below 3 V during the first charging, contrary to other reports where almost no capacity below 3 V is observed in the first cycle. A similar capacity (~ 20 mAh/g) in 2nd cycle onward is reported for NMN during cycling between 2.0-4.0 V.[61]

Figure S5(a) illustrates the rate performance of NMN and NMNT samples at different currents cycled in the 2.0-4.0 V range. The NMN shows a specific capacity of ~92, ~61, and ~2 mAh g^{-1} at 0.1C, 1C, and 5C, respectively. The corresponding values of specific capacity for NMNT are ~90, ~81, and ~68 mAh g^{-1}. While the capacity for the NMNT sample is slightly lower at 0.1 C, it shows better capacity at 1C and 5C, suggesting that Ti doping improves the rate performance. The improved rate performance is due to increased bottleneck area for Na-ion diffusion and suppressed phase transformations. Similarly, NMNT shows improved capacity retention. Figure S5(b) shows the cycling behavior of NMN and NMNT samples cycled between 2.0-4.0 V at 1C. For NMN, the capacity decreases from 61 mAh g^{-1} (first cycle) to 42.2 mAh g^{-1} (100th cycle), indicating a capacity retention of only ~69%. NMNT cathode, on the other hand, exhibited a capacity of ~ 69 mAh g^{-1} in the 100th cycle with a capacity retention of ~85% after 100 cycles.

Furthermore, the median discharge voltage decreased from 3.22 V to 3.09 V for NMNT and 3.19 V to 2.91 V for NMN after 100 cycles.

Figures 7(a) and 7(b) depict the GCD curves of NMN and NMNT at 13 mA g^{-1} in voltage range between 2.0 V and 4.5 V, respectively. Their corresponding dQ/dV versus V plots are given in Figs. 7(c) and 7(d). NMN and NMNT exhibited a first-cycle discharge capacity of ~160 mAh g^{-1} and ~141 mAh g^{-1}, respectively.

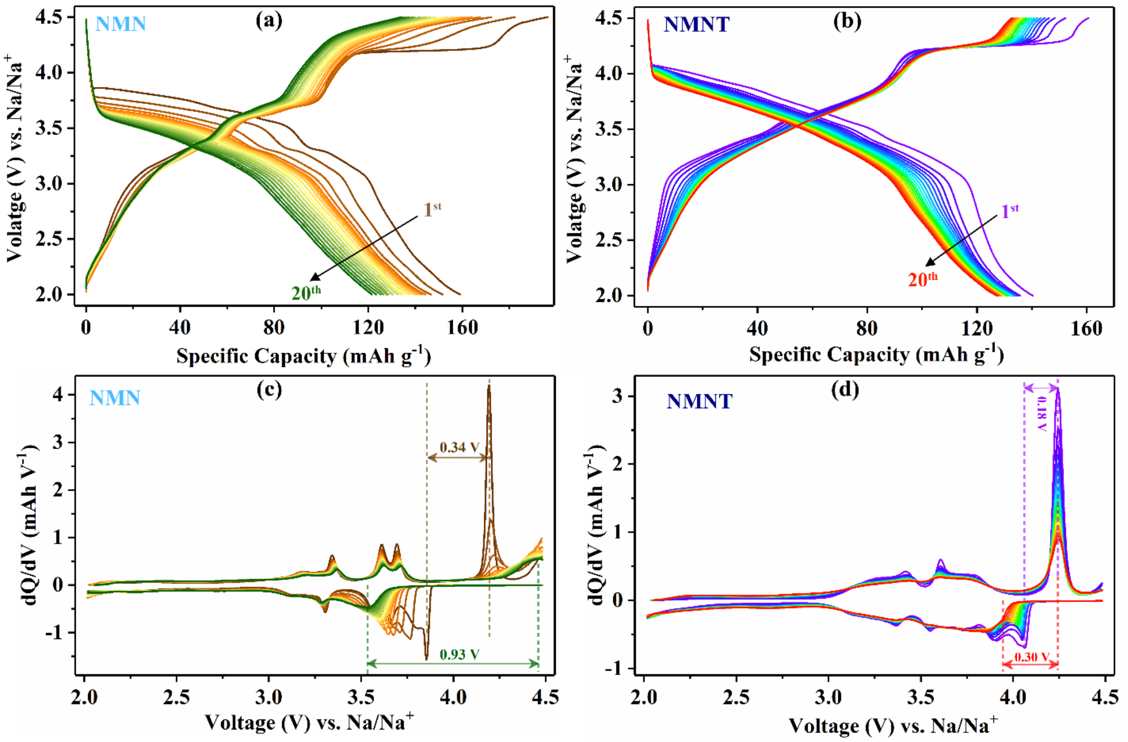

Figure 7: GCD curves of NMN (a) and NMNT (b) in the 2.0-4.5 V range at 0.1 C. The dQ/dV vs. V plots for (c) NMN and (d) NMNT.

The observed plateau at ~4.2 V (during first charging) is attributed to Ni oxidation as well as oxygen anionic redox (OAR) activity.[58, 60] OAR contribution to the overall capacity was calculated with the help of dQ/dV vs. Q plots for both samples. dQ/dV vs. V graphs show peaks corresponding to various plateaus in voltage vs. capacity plots. The voltage value at the inflection point between two peaks is used to estimate the contribution from different redox couples, as illustrated in Fig. S6. For the NMN sample, the OAR contribution was ~87 mAh g^{-1} during charging and ~67 mAh g^{-1} during discharging in the first cycle. The corresponding contribution for the NMNT sample was ~70 mAh g^{-1} during charging and ~64 mAh g^{-1} during discharging. The median discharge voltage for NMN and NMNT during the first cycle are 3.56 V and 3.59 V, respectively. The decrease in median discharge voltage after 20 cycles is much lower for NMNT (0.17 V) than for NMN (0.37 V).

A reduction in intensity is observed in OAR peaks with cycling for both samples, as can be observed from Fig. 7(c and d). Apart from a decrease in intensity, a shift in the OAR-oxidation ($O^{2-/n-}$) peak position toward higher voltage is also observed for the NMN sample. A similar shift in OAR peak towards lower voltage with cycling is observed during discharge. The polarization associated with OAR activity for NMN is ~0.34 V in the first cycle, which increases significantly to ~0.93 V after 20 cycles. Interestingly, NMNT has a much lower polarization of ~0.18 V in the first cycle, which increases only to ~0.30 V for the 20th cycle. The cycling behaviors of NMN and NMNT cathodes cycled between 2.0-4.5 V at 0.1C are shown in Fig. S7 and confirm a capacity retention of only ~ 62% after 30 cycles for NMN. NMNT exhibited a capacity of ~ 100 mAh g^{-1} in the 100th cycle with a capacity retention of ~71% after 100 cycles. The median discharge voltage decreased by 0.20 V (from 3.65 V to 3.45 V) for NMNT after 30 cycles, whereas the corresponding decrease is 0.51 V (from 3.58 V to 3.07 V) in NMN. These results show that Ti doping helps stabilize the OAR activity in NMN. It is reported that the Ti^{4+} (d^0 electronic structure) doping can reduce the oxygen loss from the lattice induced by the irreversible oxygen redox activity. [62-63] This is owing to the higher bond energy of Ti-O (662 kJ mol^{-1}) as compared to Mn-O bond energy (402 kJ mol^{-1}). [52]

The GCD profile for NMN and NMNT samples in the voltage window of 1.5-4.0 V are shown in Fig. 8(a and b). The discharge specific capacity at 0.1C for NMNT is ~149 mAh g^{-1}, marginally lower than ~153 mAh g^{-1} for the NMN. An additional plateau observed at ~2 V (during charging) corresponds to the Mn$^{3+/4+}$ activation in both samples. The 2nd cycle discharging capacities due to Mn redox activity (in 1.5-2.5 V) are ~81 mAh g^{-1} and ~66 mAh g^{-1} for NMN and NMNT, respectively. The long-term cyclability at 0.33C is better in Ti-doped samples than in NMN, as shown in Fig. 8(c). At 0.33C rate, the initial discharge capacity for NMNT is higher (~126.2 mAh g^{-1}) than that of NMN (~113.8 mAh g^{-1}). After 100 cycles, a capacity retention of ~40% and a decrease in median discharge voltage from 3.11 V to 2.67 V is observed for NMN. For NMNT, the corresponding capacity retention is ~80%, and the median discharge voltage decreases only by 0.16 V (from 3.18 V to 3.02 V). The poor cyclability in NMN is believed to be due to the cooperative Jahn-Teller distortion induced by high-spin Mn^{3+} ($t_{2g}^3e_g^1$) during electrochemical cycling. A comparison of the specific capacity and cyclability for various Ti-doped layered oxide cathodes for sodium-ion batteries is given in Table S4.

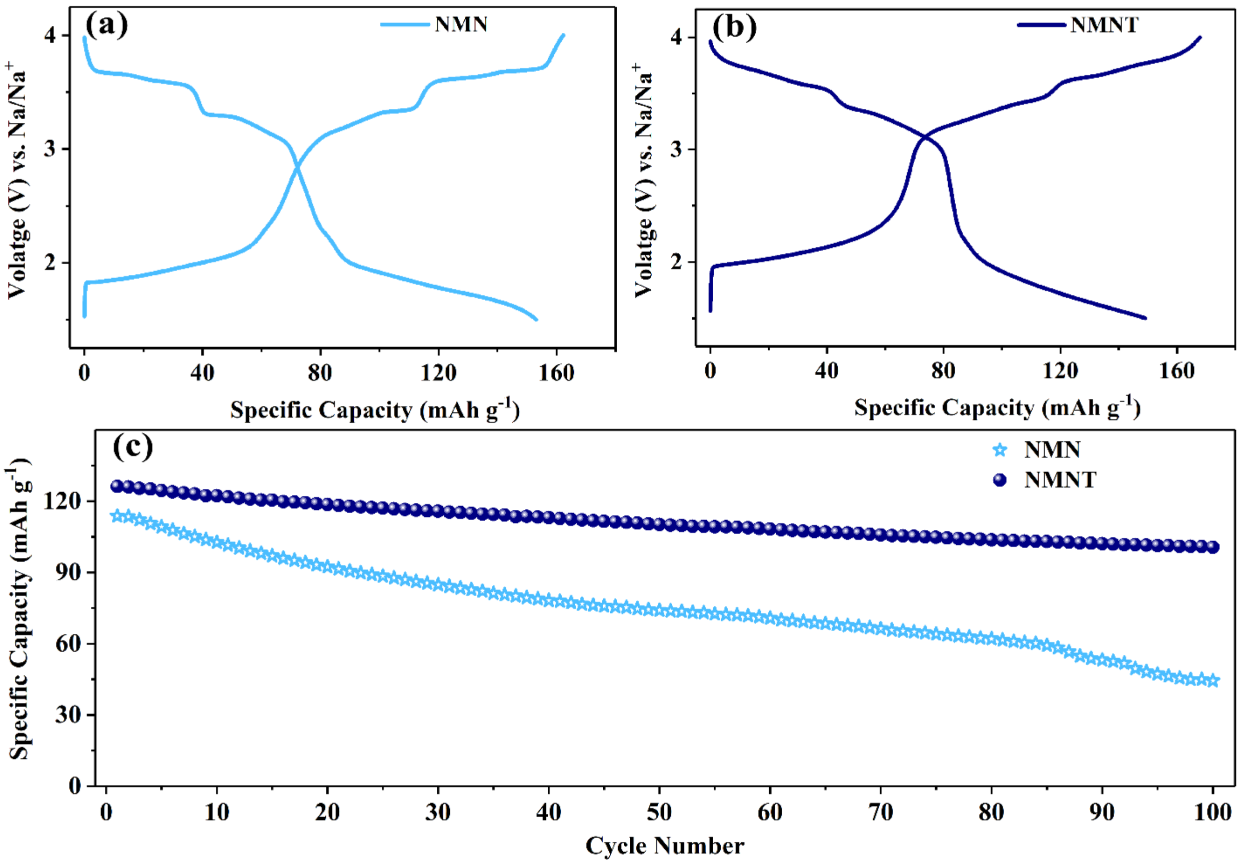

Figure 8: First cycle GCD curves of NMN (a) and NMNT (b) in 1.5 to 4.0 V range at 0.1C. (c) Cycling performance at 0.33C.

Jahn-Teller distortion in Mn-based cathode material arises due to the $Mn^{4+/3+}$ redox. When NMN is discharged to 1.5 V, a distortion in the Mn-O_6 octahedra is expected as Mn^{3+} complexes in a high spin state are known to show strong Jahn-Teller distortion effects. As both NMN and NMNT show $Mn^{4+/3+}$ redox activation when discharged to 1.5 V, it is expected that both samples should have a geometrical distortion in the Mn-O_6 octahedra in TM-O2 layers. However, the presence of larger Ti^{4+} (with a stronger Ti-O bond) in the transition metal layers suppresses the cooperative distortion of Mn-O_6 octahedra. Accordingly, the substitution of Jahn-Teller active Mn^{3+} by Ti^{4+} suppresses the structural strain and improves cycling performance. Similar impacts of inactive doping on cycling stability have been reported in other layer oxides.[64-65]

3.6. GITT

The galvanostatic intermittent titration technique (GITT) was performed to compare the room temperature Na-ions diffusion coefficients (D_{Na+}) in the NMN and NMNT cathodes at various states of charge. The results are shown in Fig. 9. These measurements were conducted during the second charge-discharge cycle and involved the application of a constant current pulse of 13 mA g^{-1} (0.1C) for 10 minutes, followed by a relaxation of 30 minutes to reach a pseudo-equilibrium state for the cathode (Fig. S8). The D_{Na+} values are calculated using the following equation (3):

$$D_{Na^+} = \frac{4}{\pi\tau}\left(\frac{m_B}{\rho S}\right)^2\left(\frac{\Delta E_S}{\Delta E_\tau}\right)^2 \qquad \left(t \ll \frac{L^2}{D}\right)$$

where ΔE_τ and ΔE_S are the voltage changes during the current pulse and when the cathode reaches equilibrium. S, ρ, m_B, and τ are the surface area of the cathode, the molar density of the cathode material, active material loading, and the duration of the constant current pulse, respectively.

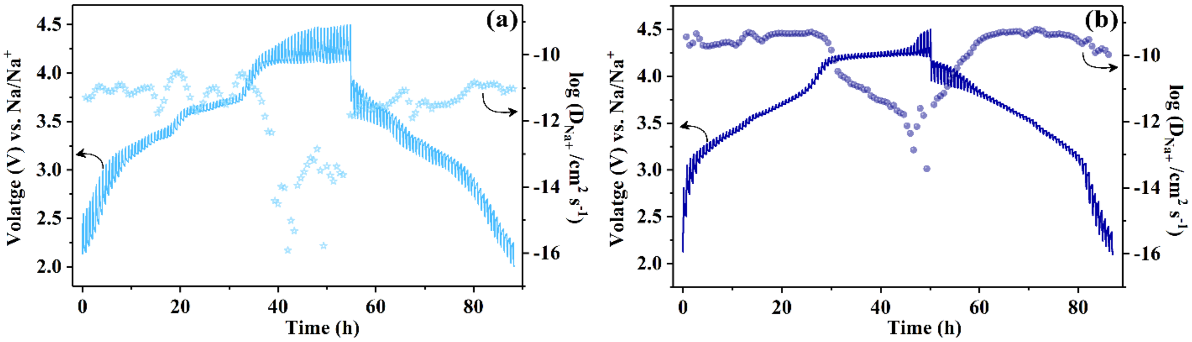

Figure 9: GITT curves and Na^+ diffusion coefficients (D_{Na+}) of (a) NMN and (b) NMNT during the charge-discharge process at 0.1C.

The GITT curves and corresponding diffusion coefficient values are presented in Fig. 9(a) for NMN and Fig. 9(b) for NMNT cathode. The values of diffusion coefficients observed for NMN are in the range of 10^{-11}-10^{-12} cm^2/s. On charging the cell above 4.0 V, the value of the diffusion coefficient starts decreasing drastically and reaches a value of ~10^{-16} cm^2/s. This decrease in D_{Na+} is due to the P2 to O2 phase transformation.[22, 66-67] In the O2-type structure, the Na-ion lies in the octahedral site, for which the triangular bottleneck area for Na-ion diffusion is much smaller than that of the rectangular bottleneck in the P2-type structure. Furthermore, the NMN is in a highly de-sodiated state when charged to 4.5 V, contributing to the low value of D_{Na+}. Figure 8(b) shows the GITT curve and the values of diffusion coefficients for the NMNT sample at various charging voltages. A trend similar to the diffusion coefficient values in NMN is also observed in Ti-doped NMN. However, the values for NMNT are 1-2 orders higher (in 2-4 V) than that of NMN. The improved Na-ion diffusion is due to the increase in the bottleneck area of the P2 structure, as confirmed by the Rietveld refinement of XRD data. It can be further seen from Fig. 9 that the diffusion coefficients are higher for NMNT than for NMN, even when the cells are charged above 4 V, suggesting that Ti doping suppresses the severity of P2 to O2 phase structural change in NMN.

To check the volume change and the phase transformation during the charge-discharge process, ex-situ XRD studies were carried out on the NMNT cathode at three different states of charge (SOC). The XRD patterns, along with LeBail fitted profiles for the cathode at 1.5 V, 4.0 V, and 4.5 V, are shown in Fig. S9. On charging the cathode from 1.5 V to 4.0 V, the (002) peak of the P2 phase shifted toward a lower angle, suggesting an increase in the lattice parameter *c*. In addition, the transition metal honeycomb ordering peaks (at 2θ ~18.5° and 20.5°), observed for NMNT discharged to 1.5 V, are absent in samples charged to 4 V and 4.5 V. The unit cell volume changed from 81.25 Å^3 for the cathode at 1.5 V to 81.35 Å3 when charged to 4.0 V. This increase in volume upon charging is expected as the sodium deintercalation increases the oxygen-oxygen layer repulsion. Interestingly, no peaks corresponding to the O2 phase are observed in the NMNT sample charged to 4.5 V. However, the FWHM of the (002) peak is substantially higher in this sample as compared to the sample charged to 4.0 V. The estimated unit cell volume for NMNT charged to 4.5 V is 81.06 Å^3. This decrease in volume and increased FWHM of (002) peak suggest a P2-to-OP4 type phase transition in the NMNT sample on charging to 4.5 V. [34]

3.7. Electrochemical impedance spectroscopy

EIS measurements at room temperature were conducted to explore the mechanism for the superior rate performance of NMNT compared to that of NMN cathode. These measurements were carried out in the 100 kHz to 10 mHz frequency range by applying a 10 mV signal. Figure 10 shows the Nyquist plots of NMN and NMNT cells. Both cells showed overlapped semi-circular arcs in the high-frequency region and a straight line in the low-frequency region. The first semicircular arc in the high-frequency region represents the interfacial layers formed on electrode surfaces. The second semicircular arc in the medium frequency region is attributed to the charge-transfer resistance. The high-frequency intercept of the semi-circular arc on the Z' axis indicates electrolyte resistance. The contribution of Na-ion diffusion in cathodes to the overall impedance appears as a straight line in the low-frequency region.

It is observed (Fig. 10) that the overall resistance of the NMN cell is higher than that of the NMNT cell. To quantify the contributions of the electrolyte resistance (R_E), interfacial layers resistance (R_{IL}), and charge-transfer resistance (R_{CT}) to the total cell resistance, an equivalent circuit modeling was employed. The equivalent circuit used to model the impedance data is shown in Fig. 10 inset. The fitted values of various parameters are given in Table S5. The table demonstrates a higher overall resistance of 1088 Ω for the NMN cell than 599 Ω for the NMNT cell. This increase is due to the higher R_{CT} value (892 Ω) in NMN than that of NMNT (386 Ω). The higher value of R_{CT} suggests that diffusion is slower in NMN than in NMNT. The GITT results also corroborate the same result. Interestingly, R_{IL} shows an increase from 191 Ω for NMN to 207 Ω for NMNT, which could be due to the higher surface area of smaller NMNT particles (as confirmed by SEM) exposed to the electrolyte. This leads to the growth of a bigger passivation layer on the surface of NMNT particles.

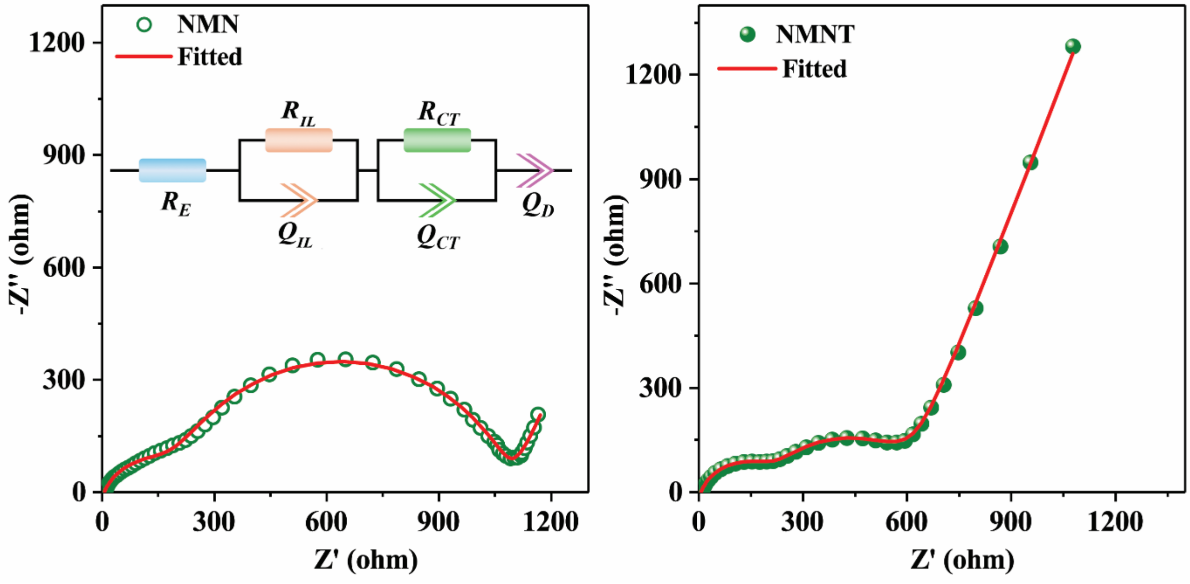

Figure 10: Room temperature experimental impedance (open circles) and fitted data (solid line) for NMN and NMNT. The equivalent circuit used for fitting is shown as the inset.

4. Conclusions

In summary, 10% Ti-substituted P2-type NMNT was synthesized via a sol-gel route, and the uniform distribution of the Ti^{4+} was confirmed by the XRD, SEM, TEM, and XPS analyses. Ti doping expanded the Na-O2 interlayer spacings and suppressed the Na^+/vacancy ordering. During cycling between 2.0 V to 4.0 V, the NMNT cathode exhibited slightly lower initial discharge capacity (~90 mAh g^{-1} at 0.1C) but showed better rate performance, cyclability, and higher nominal voltage than undoped NMN. Furthermore, the severe capacity fading in NMN attributed to the irreversible anionic redox, when charged to 4.5 V, was tremendously stabilized by the Ti acting as pillar-ions. The stabilization of anionic redox, better rate performance, and improved cyclability in the NMNT sample are attributed to the stronger Ti-O bond, increased disorder, and the suppression of cooperative Jahn-Teller distortion.

Supporting Information

XRD patterns and FTIR spectra of pristine and ambient-air exposed samples; SEM images and EDS elemental mappings; Na 1s & Ti 2p XPS spectra and Rate performance & cyclability data for NMN and NMNT; Estimation of OAR contribution plot; Illustration of the single titration unit of GITT during charging; Ex-situ XRD patterns of NMNT cathode at different states of charge.

Acknowledgments

This work was financially supported by the Ministry of Education (grant number: MoE-STARS/STARS-2/2023-0365) and the Science and Engineering Research Board (grant number: CRG/2021/005548), Government of India. ND acknowledges the UGC-JRF scheme of the Government of India (Grant no. 231610004459). This research utilized the Transmission Electron Microscope (TEM) in the Boise State University FaCT Core Facility, RRID: SCR_024733, which receives support from the National Institutes of Health [NIH] under the Institutional Development Awards [IDeA] Program of the National Institute of General Medical Sciences [NIGMS] via grants P20GM148321 and P20GM103408.

Conflict of interest statement

The authors declare no conflict of interest.

REFERENCES

1. Hirsh, H. S.; Li, Y.; Tan, D. H. S.; Zhang, M.; Zhao, E.; Meng, Y. S., Sodium-Ion Batteries Paving the Way for Grid Energy Storage. *Adv. Energy Mater.* **2020,** *10* (32), 2001274.

2. Zhu, Z.; Jiang, T.; Ali, M.; Meng, Y.; Jin, Y.; Cui, Y.; Chen, W., Rechargeable Batteries for Grid Scale Energy Storage. *Chem. Rev.* **2022,** *122* (22), 16610-16751.

3. Manthiram, A., A reflection on lithium-ion battery cathode chemistry. *Nat. Commun.* **2020,** *11* (1), 1550.

4. Delmas, C., Sodium and Sodium-Ion Batteries: 50 Years of Research. *Adv. Energy Mater.* **2018,** *8* (17), 1703137.

5. Yabuuchi, N.; Kubota, K.; Dahbi, M.; Komaba, S., Research Development on Sodium-Ion Batteries. *Chem. Rev.* **2014,** *114* (23), 11636-11682.

6. Liu, X.; Xiao, B.; Daali, A.; Zhou, X.; Yu, Z.; Li, X.; Liu, Y.; Yin, L.; Yang, Z.; Zhao, C.; Zhu, L.; Ren, Y.; Cheng, L.; Ahmed, S.; Chen, Z.; Li, X.; Xu, G.-L.; Amine, K., Stress- and Interface-Compatible Red Phosphorus Anode for High-Energy and Durable Sodium-Ion Batteries. *ACS Energy Lett.* **2021,** *6* (2), 547-556.

7. Tapia-Ruiz, N.; Armstrong, A. R.; Alptekin, H.; Amores, M. A.; Au, H.; Barker, J.; Boston, R.; Brant, W. R.; Brittain, J. M.; Chen, Y.; Chhowalla, M.; Choi, Y.-S.; Costa, S. I. R.; Crespo Ribadeneyra, M.; Cussen, S. A.; Cussen, E. J.; David, W. I. F.; Desai, A. V.; Dickson, S. A. M.; Eweka, E. I.; Forero-Saboya, J. D.; Grey, C. P.; Griffin, J. M.; Gross, P.; Hua, X.; Irvine, J. T. S.; Johansson, P.; Jones, M. O.; Karlsmo, M.; Kendrick, E.; Kim, E.; Kolosov, O. V.; Li, Z.; Mertens, S. F. L.; Mogensen, R.; Monconduit, L.; Morris, R. E.; Naylor, A. J.; Nikman, S.; O'Keefe, C. A.; Ould, D. M. C.; Palgrave, R. G.; Poizot, P.; Ponrouch, A.; Renault, S.; Reynolds, E. M.; Rudola, A.; Sayers, R.; Scanlon, D. O.; Sen, S.; Seymour, V. R.; Silván, B.; Sougrati, M. T.; Stievano, L.; Stone, G. S.; Thomas, C. I.; Titirici, M.-M.; Tong, J.; Wood, T. J.; Wright, D. S.; Younesi, R., 2021 roadmap for sodium-ion batteries. *J. Phys. Energy* **2021,** *3* (3), 031503.

8. Rudola, A.; Sayers, R.; Wright, C. J.; Barker, J., Opportunities for moderate-range electric vehicles using sustainable sodium-ion batteries. *Nat. Energy* **2023,** *8* (3), 215-218.

9. Rudola, A.; Rennie, A. J. R.; Heap, R.; Meysami, S. S.; Lowbridge, A.; Mazzali, F.; Sayers, R.; Wright, C. J.; Barker, J., Commercialisation of high energy density sodium-ion batteries: Faradion's journey and outlook. *J. Mater. Chem. A* **2021,** *9* (13), 8279-8302.

10. Barpanda, P.; Lander, L.; Nishimura, S.-i.; Yamada, A., Polyanionic Insertion Materials for Sodium-Ion Batteries. *Adv. Energy Mater.* **2018,** *8* (17), 1703055.

11. Peng, J.; Zhang, W.; Liu, Q.; Wang, J.; Chou, S.; Liu, H.; Dou, S., Prussian Blue Analogues for Sodium-Ion Batteries: Past, Present, and Future. *Adv. Mater.* **2022,** *34* (15), 2108384.

12. Zhou, Q.; Wang, L.; Li, W.; Zhao, K.; Liu, M.; Wu, Q.; Yang, Y.; He, G.; Parkin, I. P.; Shearing, P. R.; Brett, D. J. L.; Zhang, J.; Sun, X., Sodium Superionic Conductors (NASICONs) as Cathode Materials for Sodium-Ion Batteries. *Electrochem. Energy Rev.* **2021,** *4* (4), 793-823.

13. Vasavan, H. N.; Badole, M.; Saxena, S.; Srihari, V.; Das, A. K.; Gami, P.; Deswal, S.; Kumar, P.; Kumar, S., Unveiling the potential of P3 phase in enhancing the electrochemical performance of a layered oxide cathode. *Mater. Today Energy* **2023,** *37*, 101380.

14. Wang, P.-F.; You, Y.; Yin, Y.-X.; Guo, Y.-G., Layered Oxide Cathodes for Sodium-Ion Batteries: Phase Transition, Air Stability, and Performance. *Adv. Energy Mater.* **2018,** *8* (8), 1701912.

15. Vasavan, H. N.; Badole, M.; Saxena, S.; Srihari, V.; Das, A. K.; Gami, P.; Deswal, S.; Kumar, P.; Kumar, S., Impact of P3/P2 mixed phase on the structural and electrochemical performance of $Na_{0.75}Mn_{0.75}Al_{0.25}O_2$ cathode. *J. Energy Storage* **2023,** *74*, 109428.

16. Saxena, S.; Vasavan, H. N.; Badole, M.; Das, A. K.; Deswal, S.; Kumar, P.; Kumar, S., Tailored P2/O3 phase-dependent electrochemical behavior of Mn-based cathode for sodium-ion batteries. *J. Energy Storage* **2023,** *64*, 107242.

17. Vasavan, H. N.; Badole, M.; Saxena, S.; Srihari, V.; Das, A. K.; Gami, P.; Dagar, N.; Deswal, S.; Kumar, P.; Poswal, H. K.; Kumar, S., Rational design of an optimal Al-

substituted layered oxide cathode for Na-ion batteries. *Electrochim. Acta* **2024,** *494*, 144457.

18. Saxena, S.; Badole, M.; Vasavan, H. N.; Srihari, V.; Das, A. K.; Gami, P.; Deswal, S.; Kumar, P.; Kumar, S., Deciphering the role of optimal P2/O3 phase fraction in enhanced cyclability and specific capacity of layered oxide cathodes. *Chem. Eng. J.* **2024,** *485*, 149921.

19. Zhang, J.; Wang, W.; Wang, W.; Wang, S.; Li, B., Comprehensive Review of P2-Type $Na_{2/3}Ni_{1/3}Mn_{2/3}O_2$, a Potential Cathode for Practical Application of Na-Ion Batteries. *ACS Appl. Mater. Interfaces* **2019,** *11* (25), 22051-22066.

20. Saxena, S.; Badole, M.; Vasavan, H. N.; Srihari, V.; Das, A. K.; Gami, P.; Dagar, N.; Deswal, S.; Kumar, P.; Poswal, H. K.; Kumar, S., Elucidating the Electrochemical Behavior of a P3-type High-Na-Content Cathode. *Energy Fuels* **2024,** *38* (13), 12140-12149.

21. Risthaus, T.; Chen, L.; Wang, J.; Li, J.; Zhou, D.; Zhang, L.; Ning, D.; Cao, X.; Zhang, X.; Schumacher, G.; Winter, M.; Paillard, E.; Li, J., P3 $Na_{0.9}Ni_{0.5}Mn_{0.5}O_2$ Cathode Material for Sodium Ion Batteries. *Chem. Mater.* **2019,** *31* (15), 5376-5383.

22. Yoshida, H.; Yabuuchi, N.; Kubota, K.; Ikeuchi, I.; Garsuch, A.; Schulz-Dobrick, M.; Komaba, S., P2-type $Na_{2/3}Ni_{1/3}Mn_{2/3-x}Ti_xO_2$ as a new positive electrode for higher energy Na-ion batteries. *Chem. Commun.* **2014,** *50* (28), 3677-3680.

23. Dagar, N.; Saxena, S.; Vasavan, H. N.; Das, A. K.; Gami, P.; Deswal, S.; Kumar, P.; Kumar, S., Distinct electrochemical behavior of P3 and P2 polytypes of Mn/Ni-based Na-ion battery cathode. *Mater. Lett.* **2024,** *369*, 136768.

24. Yu, F.; Zhang, S.; Fang, C.; Liu, Y.; He, S.; Xia, J.; Yang, J.; Zhang, N., Electrochemical characterization of P2-type layered $Na_{2/3}Ni_{1/4}Mn_{3/4}O_2$ cathode in aqueous hybrid sodium/lithium ion electrolyte. *Ceram. Int.* **2017,** *43* (13), 9960-9967.

25. Liu, C.-Z.; Liu, M.-Z.; Cheng, Z.-X.; Ren, K.-R.; Wang, P.-F.; Liu, Z.-L.; Shu, J.; Yi, T.-F., Mo-based compounds coating to stabilize Mn-based layered oxide cathode material towards high-performance Na-ion batteries with ultrahigh cycling stability. *Ceram. Int.* **2024,** *50* (13, Part B), 24397-24405.

26. Venkatesh, M.; Priyanga, G. S.; Sharma, S.; Kanta, P. L. M.; Thomas, T.; Gopalan, R.; Das, B., Effect of dopants and microstructure on the electrochemical cyclic stability of layered P2-type $Na_{0.67}MnO_2$ prepared by different chemical routes: An experimental and theoretical study. *Ceram. Int.* **2023,** *49* (4), 6654-6665.

27. Delmas, C.; Fouassier, C.; Hagenmuller, P., Structural classification and properties of the layered oxides. *Physica B+C* **1980,** *99* (1), 81-85.

28. Clément, R. J.; Bruce, P. G.; Grey, C. P., Review—Manganese-Based P2-Type Transition Metal Oxides as Sodium-Ion Battery Cathode Materials. *J. Electrochem. Soc.* **2015,** *162* (14), A2589.

29. Zhao, C.; Yao, Z.; Wang, Q.; Li, H.; Wang, J.; Liu, M.; Ganapathy, S.; Lu, Y.; Cabana, J.; Li, B.; Bai, X.; Aspuru-Guzik, A.; Wagemaker, M.; Chen, L.; Hu, Y.-S., Revealing High Na-Content P2-Type Layered Oxides as Advanced Sodium-Ion Cathodes. *J. Am. Chem. Soc.* **2020,** *142* (12), 5742-5750.

30. Hu, H.-Y.; Li, J.-Y.; Liu, Y.-F.; Zhu, Y.-F.; Li, H.-W.; Jia, X.-B.; Jian, Z.-C.; Liu, H.-X.; Kong, L.-Y.; Li, Z.-Q.; Dong, H.-H.; Zhang, M.-K.; Qiu, L.; Wang, J.-Q.; Chen, S.-Q.; Wu, X.-W.; Guo, X.-D.; Xiao, Y., Developing an abnormal high-Na-content P2-type layered oxide cathode with near-zero-strain for high-performance sodium-ion batteries. *Chem. Sci.* **2024,** *15* (14), 5192-5200.

31. Anilkumar, A.; Nair, N.; Nair, S. V.; Baskar, S., Tailoring high Na content in P2-type layered oxide cathodes via CuLi dual doping for sodium-ion batteries. *J. Energy Storage* **2023,** *72*, 108291.

32. Lu, Z.; Dahn, J. R., In Situ X-Ray Diffraction Study of P2 $Na_{2/3}[Ni_{1/3}Mn_{2/3}]O_2$. *J. Electrochem. Soc.* **2001,** *148* (11), A1225.

33. Li, Y.; Mazzio, K. A.; Yaqoob, N.; Sun, Y.; Freytag, A. I.; Wong, D.; Schulz, C.; Baran, V.; Mendez, A. S. J.; Schuck, G.; Zając, M.; Kaghazchi, P.; Adelhelm, P., Competing Mechanisms Determine Oxygen Redox in Doped Ni–Mn Based Layered Oxides for Na-Ion Batteries. *Adv. Mater.* **2024,** *36* (18), 2309842.

34. Kubota, K.; Asari, T.; Komaba, S., Impact of Ti and Zn Dual-Substitution in P2 Type $Na_{2/3}Ni_{1/3}Mn_{2/3}O_2$ on Ni–Mn and Na-Vacancy Ordering and Electrochemical Properties. *Adv. Mater.* **2023,** *35* (26), 2300714.

35. Cheng, C.; Hu, H.; Yuan, C.; Xia, X.; Mao, J.; Dai, K.; Zhang, L., Precisely modulating the structural stability and redox potential of sodium layered cathodes through the synergetic effect of co-doping strategy. *Energy Storage Mater.* **2022,** *52*, 10-18.

36. Ding, F.; Zhao, C.; Xiao, D.; Rong, X.; Wang, H.; Li, Y.; Yang, Y.; Lu, Y.; Hu, Y.-S., Using High-Entropy Configuration Strategy to Design Na-Ion Layered Oxide Cathodes with Superior Electrochemical Performance and Thermal Stability. *J. Am. Chem. Soc.* **2022,** *144* (18), 8286-8295.

37. Wang, Q.; Yu, G.; Luo, B.; Ji, W.; Liu, Z.; Li, M.; Nong, Y.; Tian, Y.; Wang, X.; Zhang, J.; Chen, C.-L.; Chang, C.-K.; Sang, Z.; Zhao, Z.; Zhao, R.; Liang, J., Suppression of Adverse Phase Transition of Layered Oxide Cathode via Local Electronic Structure Regulation for High-Capacity Sodium-Ion Batteries. *ACS Nano* **2024,** *18* (28), 18622-18634.

38. Hwang, J.-Y.; Kim, J.; Yu, T.-Y.; Sun, Y.-K., A New P2-Type Layered Oxide Cathode with Extremely High Energy Density for Sodium-Ion Batteries. *Adv. Energy Mater.* **2019,** *9* (15), 1803346.

39. Tang, K.; Huang, Y.; Xie, X.; Cao, S.; Liu, L.; Liu, H.; Luo, Z.; Wang, Y.; Chang, B.; Shu, H.; Wang, X., Electrochemical performance and structural stability of air-stable $Na_{0.67}Ni_{0.33}Mn_{0.67-x}Ti_xO_2$ cathode materials for high-performance sodium-ion batteries. *Chem. Eng. J.* **2020,** *399*, 125725.

40. Zhang, X.; Zuo, W.; Liu, S.; Zhao, C.; Li, Q.; Gao, Y.; Liu, X.; Xiao, D.; Hwang, I.; Ren, Y.; Sun, C.-J.; Chen, Z.; Wang, B.; Feng, Y.; Yang, W.; Xu, G.-L.; Amine, K.; Yu, H., High-Energy Earth-Abundant Cathodes with Enhanced Cationic/Anionic Redox for Sustainable and Long-Lasting Na-Ion Batteries. *Adv. Mater.* **2024,** *36* (33), 2310659.

41. Wang, P. F.; Yao, H. R.; Liu, X. Y.; Yin, Y. X.; Zhang, J. N.; Wen, Y.; Yu, X.; Gu, L.; Guo, Y. G., Na^+/vacancy disordering promises high-rate Na-ion batteries. *Sci. Adv.* **2018,** *4* (3), eaar6018.

42. Zhou, J.; Hu, H.; Wang, J.; Shi, Q.; Lian, X.; Liu, L.; Bachmatiuk, A.; Sun, J.; Yang, R.; Choi, J.-H.; Rümmeli, M. H., Titanium Substitution Facilitating Oxygen and

Manganese Redox in Sodium Layered Oxide Cathode. *Adv. Mater. Interfaces* **2024,** *11* (22), 2400190.

43. Zhao, S.; Shi, Q.; Feng, W.; Liu, Y.; Yang, X.; Zou, X.; Lu, X.; Zhao, Y., Suppression of multistep phase transitions of O3-type cathode for sodium-ion batteries. *Chin. Chem. Lett.* **2024,** *35* (5), 108606.

44. Xie, Z.-Y.; Xing, X.; Yu, L.; Chang, Y.-X.; Yin, Y.-X.; Xu, L.; Yan, M.; Xu, S., Mg/Ti doping co-promoted high-performance P2-$Na_{0.67}Ni_{0.28}Mg_{0.05}Mn_{0.62}Ti_{0.05}O_2$ for sodium-ion batteries. *Appl. Phys. Lett.* **2022,** *121* (20), 203903.

45. Vasavan, H. N.; Badole, M.; Dwivedi, S.; Kumar, D.; Kumar, P.; Kumar, S., Enhanced rate performance and specific capacity in Ti-substituted P2-type layered oxide enabled by crystal structure and particle morphology modifications. *Chem. Eng. J.* **2022,** *448*, 137662.

46. Vasavan, H. N.; Badole, M.; Saxena, S.; Das, A. K.; Deswal, S.; Kumar, P.; Kumar, S., Excellent Structural Stability-Driven Cyclability in P2-Type Ti-Based Cathode for Na-Ion Batteries. *ACS Appl. Energy Mater.* **2023,** *6* (4), 2440-2447.

47. Vasavan, H. N.; Badole, M.; Dwivedi, S.; Kumar, S., Structural and transport properties of P2-Type $Na_{0.70}Ni_{0.20}Cu_{0.15}Mn_{0.65}O_2$ layered oxide. *Ceram. Int.* **2022,** *48* (s19), 28986-28993.

48. Peck, M. A.; Langell, M. A., Comparison of Nanoscaled and Bulk NiO Structural and Environmental Characteristics by XRD, XAFS, and XPS. *Chem. Mater.* **2012,** *24* (23), 4483-4490.

49. Wang, P.-F.; Yao, H.-R.; Liu, X.-Y.; Zhang, J.-N.; Gu, L.; Yu, X.-Q.; Yin, Y.-X.; Guo, Y.-G., Ti-Substituted NaNi0.5Mn0.5-TiO2 Cathodes with Reversible O3−P3 Phase Transition for High-Performance Sodium-Ion Batteries. *Adv. Mater.* **2017,** *29* (19), 1700210.

50. Yang, T.; Chen, N.; Li, A.; Feng, A.; Li, Y.; Qin, Y.; Qin, X.; Shi, C., Enhancement of electrochemical performance of sodium-ion battery cathode material $Na_{0.67}Ni_{0.33}Mn_{0.67}O_2$ by Zn/Al co-substitution. *Inorg. Chem. Commun.* **2025,** *173*, 113874.

51. Coelho, A., TOPAS and TOPAS-Academic: an optimization program integrating computer algebra and crystallographic objects written in C++. *J. Appl. Crystallogr.* **2018,** *51* (1), 210-218.

52. Shannon, R. D.; Prewitt, C. T., Effective ionic radii in oxides and fluorides. *Acta. Crystallogr. B.* **1969,** *25* (5), 925-946.

53. Yi, H.; Li, Z.; Li, X.; Gao, P.; Zhu, Y., Ti-Substituted O3-$NaNi_{0.5}Mn_{0.3}Ti_{0.2}O_2$ Material with a Disordered Transition Metal Layer and a Stable Structure. *ACS Appl. Mater. Interfaces* **2024,** *16* (33), 43636-43646.

54. Sengupta, A.; Kumar, A.; Barik, G.; Ahuja, A.; Ghosh, J.; Lohani, H.; Kumari, P.; Bhandakkar, T. K.; Mitra, S., Lower Diffusion-Induced Stress in Nano-Crystallites of P2-$Na_{2/3}Ni_{1/3}Mn_{1/2}Ti_{1/6}O_2$ Novel Cathode for High Energy Na-ion Batteries. *Small* **2023,** *19* (12), 2206248.

55. Schneider, C. A.; Rasband, W. S.; Eliceiri, K. W., NIH Image to ImageJ: 25 years of image analysis. *Nat. Methods* **2012,** *9* (7), 671-675.

56. Shi, Y.; Jiang, P.; Wang, S.; Chen, W.; Wei, B.; Lu, X.; Qian, G.; Kan, W. H.; Chen, H.; Yin, W.; Sun, Y.; Lu, X., Slight compositional variation-induced structural disorder-to-order transition enables fast Na+ storage in layered transition metal oxides. *Nat. Commun.* **2022,** *13* (1), 7888.

57. Fang, D.; Li, J., Regulating Interfacial Compositions to Build a Stable Superlattice Structure of Layered Oxide Cathode Materials for Sodium-Ion Batteries. *ACS Appl. Energy Mater.* **2024,** *7* (10), 4639-4649.

58. Yeh, C.-H.; Kang, J.-W.; Chen, Y.-L.; Chen, H.-J.; Chang, H.-H.; Lu, W.-H.; Chen, S.-Y.; Chen, H.-L.; Hu, C.-W.; Chueh, L.-Y.; Pan, Y.-T. F.; Chen, H.-Y., Electrochemical Improvement of $Na_{0.62}K_{0.05}Mg_{2/9}Cu_{1/9}Mn_{2/3}O_2$ P2-Type Layer-Oxide Anionic Redox Cathodes of Sodium-Ion Batteries via Incorporating K-Doping. *ACS Sustain. Chem. Eng.* **2024,** *12* (34), 12795-12807.

59. Delmas, C.; Braconnier, J.-J.; Fouassier, C.; Hagenmuller, P., Electrochemical intercalation of sodium in Na_xCoO_2 bronzes. *Solid State Ion.* **1981,** *3-4*, 165-169.

60. Chen, B.; Xin, Y.; Wang, Y.; Ding, X.; Jiang, C.; Wu, F.; Gao, H., Modulating the oxygen redox activity of an ultra-high capacity P3 type cathode for sodium-ion batteries via beryllium introduced. *Energy Storage Mater.* **2024,** *67*, 103252.

61. Wang, H.; Yang, B.; Liao, X.-Z.; Xu, J.; Yang, D.; He, Y.-S.; Ma, Z.-F., Electrochemical properties of P2-$Na_{2/3}[Ni_{1/3}Mn_{2/3}]O_2$ cathode material for sodium ion batteries when cycled in different voltage ranges. *Electrochim. Acta* **2013,** *113*, 200-204.

62. Cao, X.; Li, X.; Qiao, Y.; Jia, M.; Qiu, F.; He, Y.; He, P.; Zhou, H., Restraining Oxygen Loss and Suppressing Structural Distortion in a Newly Ti-Substituted Layered Oxide P2-$Na_{0.66}Li_{0.22}Ti_{0.15}Mn_{0.63}O_2$. *ACS Energy Lett.* **2019,** *4* (10), 2409-2417.

63. Li, C.; Zhao, C.; Hu, B.; Tong, W.; Shen, M.; Hu, B., Unraveling the Critical Role of Ti Substitution in P2-$Na_xLi_yMn_{1-y}O_2$ Cathodes for Highly Reversible Oxygen Redox Chemistry. *Chem. Mater.* **2020,** *32* (3), 1054-1063.

64. Fang, T.; Guo, S.; Jiang, K.; Zhang, X.; Wang, D.; Feng, Y.; Zhang, X.; Wang, P.; He, P.; Zhou, H., Revealing the Critical Role of Titanium in Layered Manganese-Based Oxides toward Advanced Sodium-Ion Batteries via a Combined Experimental and Theoretical Study. *Small Methods* **2019,** *3* (4), 1800183.

65. Ramasamy, H. V.; Kaliyappan, K.; Thangavel, R.; Seong, W. M.; Kang, K.; Chen, Z.; Lee, Y.-S., Efficient Method of Designing Stable Layered Cathode Material for Sodium Ion Batteries Using Aluminum Doping. *J. Phys. Chem. Lett.* **2017,** *8* (20), 5021-5030.

66. Wu, X.; Xu, G.-L.; Zhong, G.; Gong, Z.; McDonald, M. J.; Zheng, S.; Fu, R.; Chen, Z.; Amine, K.; Yang, Y., Insights into the Effects of Zinc Doping on Structural Phase Transition of P2-Type Sodium Nickel Manganese Oxide Cathodes for High-Energy Sodium Ion Batteries. *ACS Appl. Mater. Interfaces* **2016,** *8* (34), 22227-22237.

67. Lee, D. H.; Xu, J.; Meng, Y. S., An advanced cathode for Na-ion batteries with high rate and excellent structural stability. *Phys. Chem. Chem. Phys.* **2013,** *15* (9), 3304-3312.

[Supporting Information]

Ti-substitution Facilitating Anionic Redox and Cycle Stability in P2-type $Na_{2/3}Mn_{2/3}Ni_{1/3}O_2$ Na-ion Battery Cathode

Neha Dagar[1], Samriddhi Saxena[1], Hari Narayanan Vasavan[1], Asish Kumar Das[1], Pratiksha Gami[1], Sonia Deswal[2], Pradeep Kumar[2], Karthik Chinnathambi[3], Vikram Rathee[4], and Sunil Kumar[1,]*

[1]*Department of Metallurgical Engineering and Materials Science, Indian Institute of Technology Indore, Simrol, 453552, India*

[2]*School of Physical Sciences, Indian Institute of Technology Mandi, Mandi, 175005, India*

[3]*Micron School of Materials Science and Engineering, Boise State University, Boise, ID 83725, USA*

[4]*Department of Physics and Astrophysics, Delhi University, Delhi, 110007, India*

*sunil@iiti.ac.in

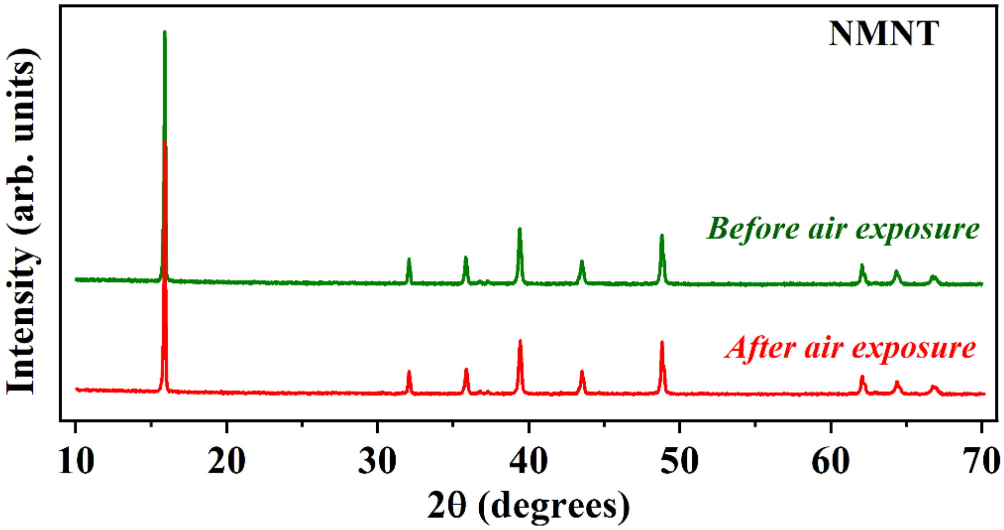

Figure S1: XRD patterns of as-prepared NMNT sample (before air exposure) and after exposing the sample to ambient air for 30 days

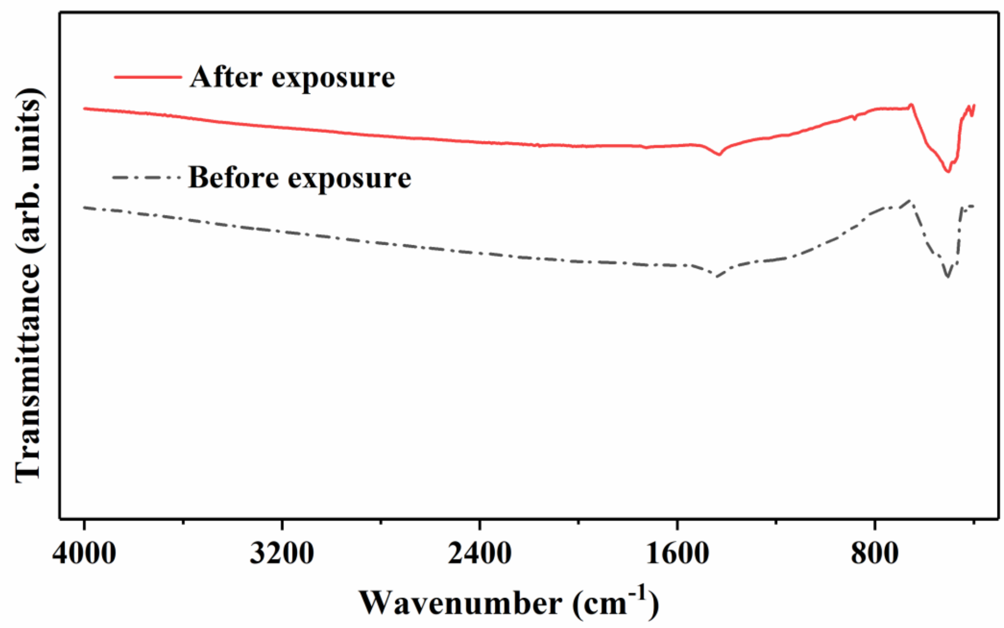

Figure S2: FTIR spectra of as-prepared (before exposure)NMNT sample and after exposing the sample to ambient air for 30 days

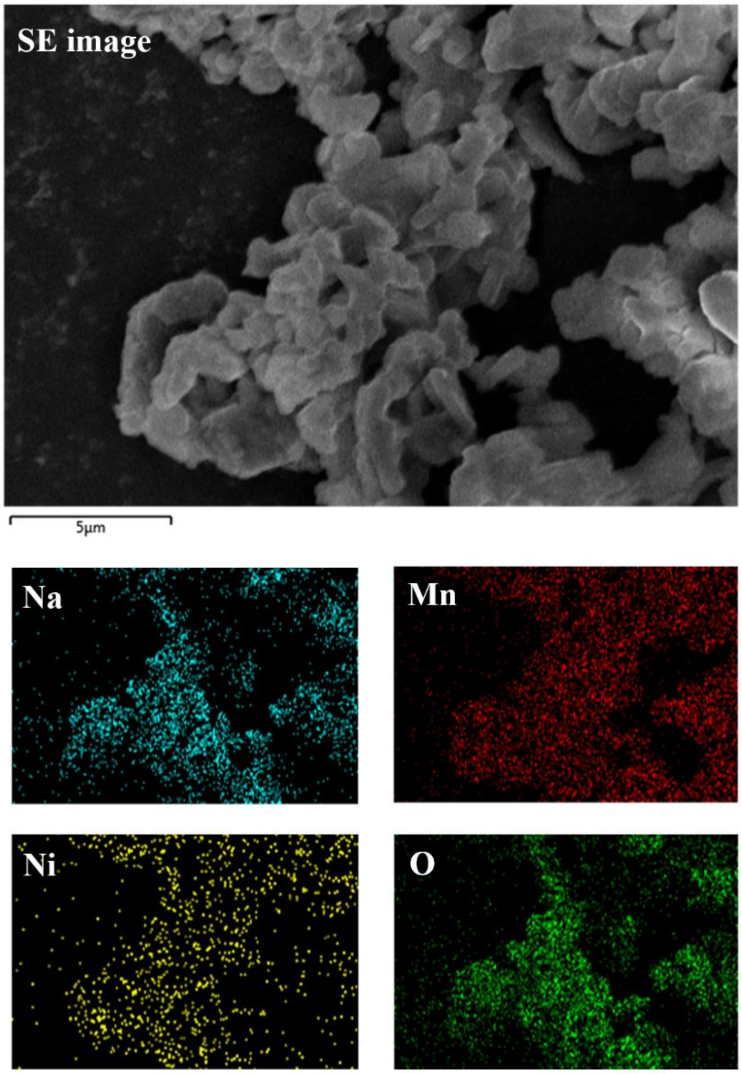

Figure S3: EDS elemental mappings for NMN sample.

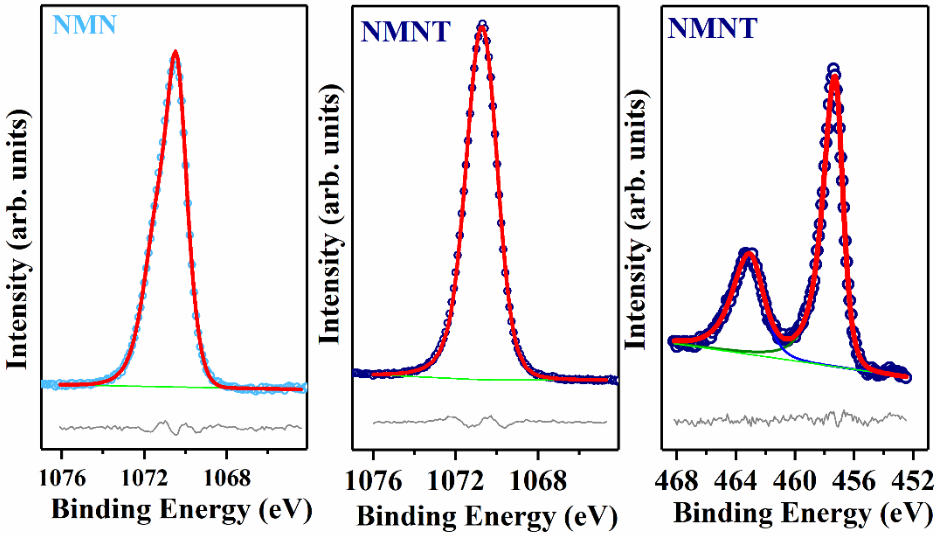

Figure S4: Na 1s (of NMN and NMNT samples) and Ti 2p XPS spectra for NMNT.

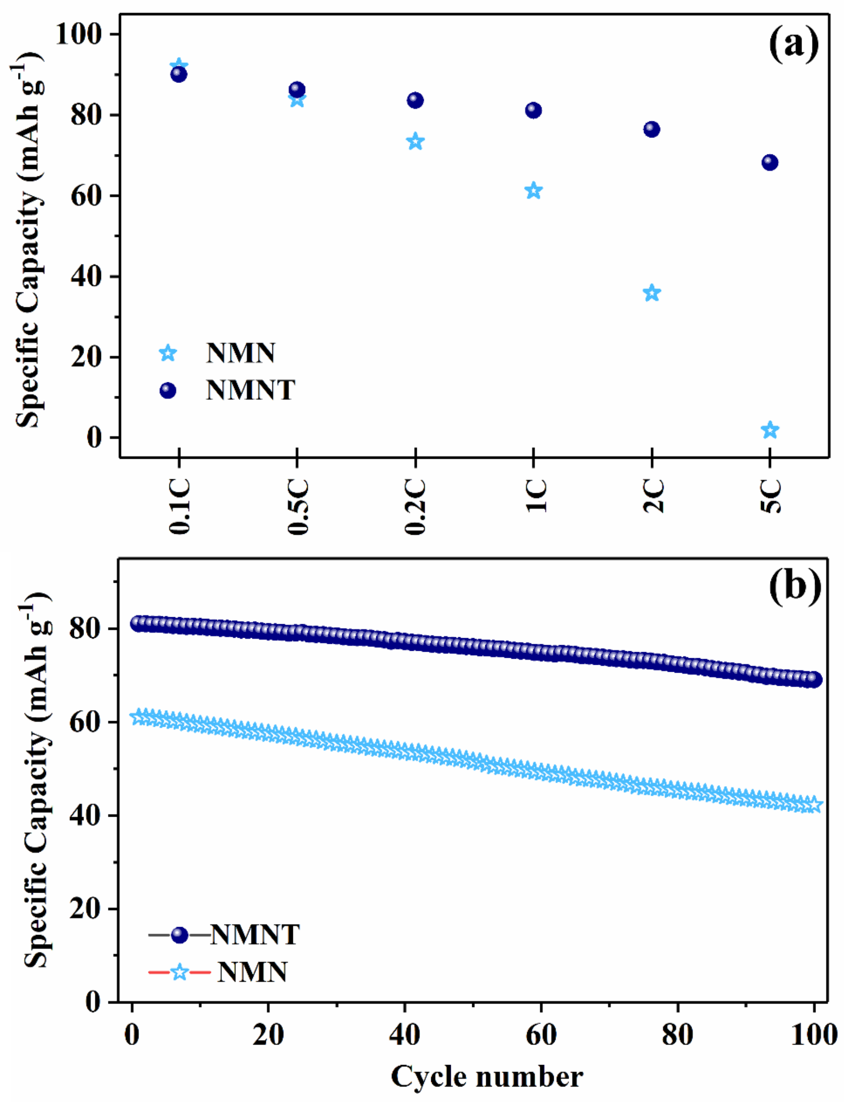

Figure S5: (a) Specific capacity at various C-rates for NMN and NMNT samples. (b) Cycling stability of NMN and NMNT in the 2.0-4.0 V range at 1C.

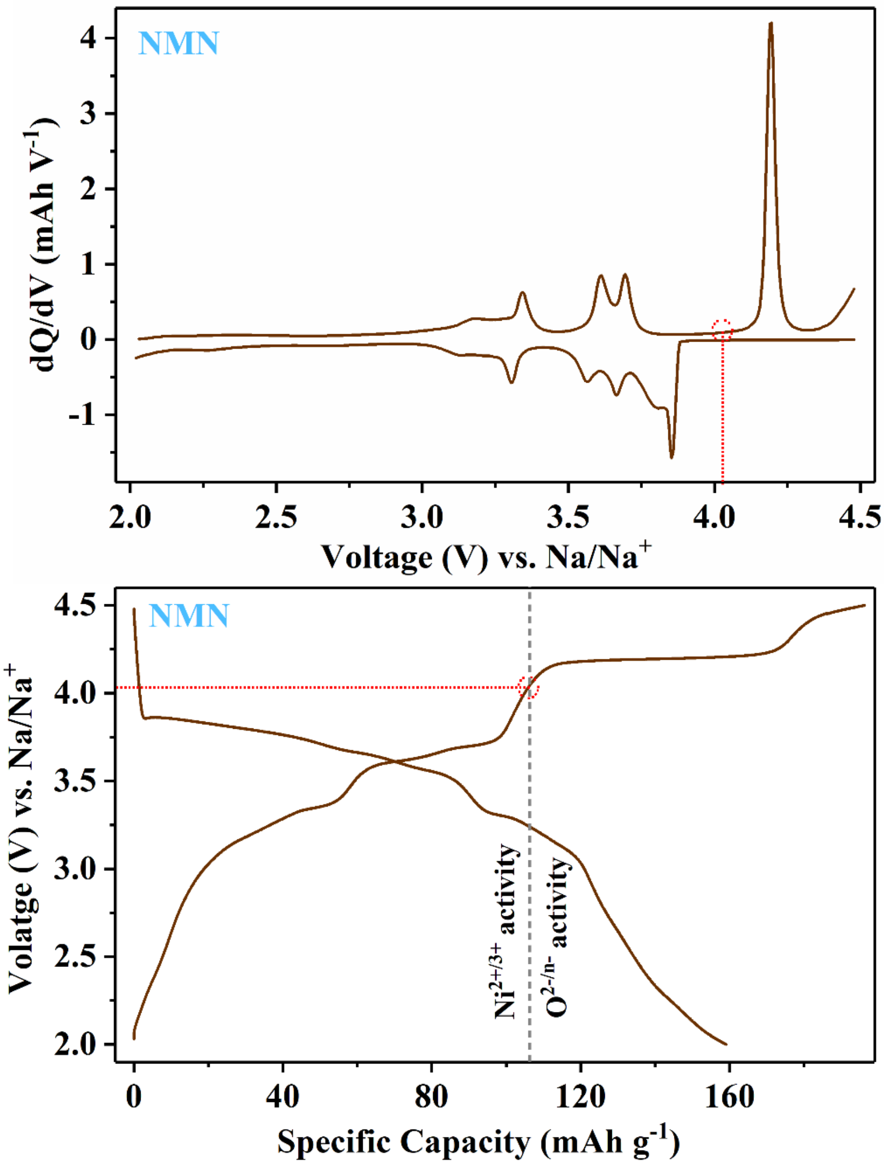

Figure S6: The dQ/dV vs. V and voltage vs. specific capacity plots for the estimation of the oxygen redox activity contribution to the total capacity.

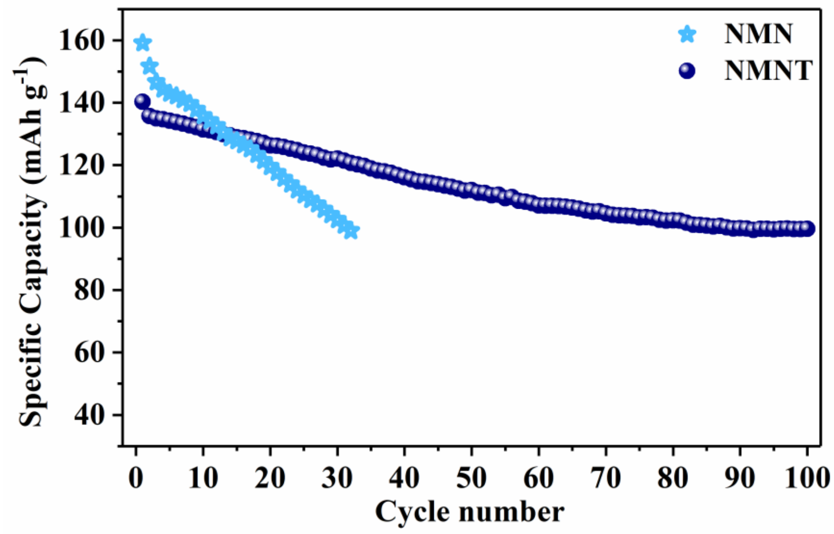

Figure S7: Cycling stability of NMN and NMNT cycled in the 2.0-4.5 V range at 0.1 C.

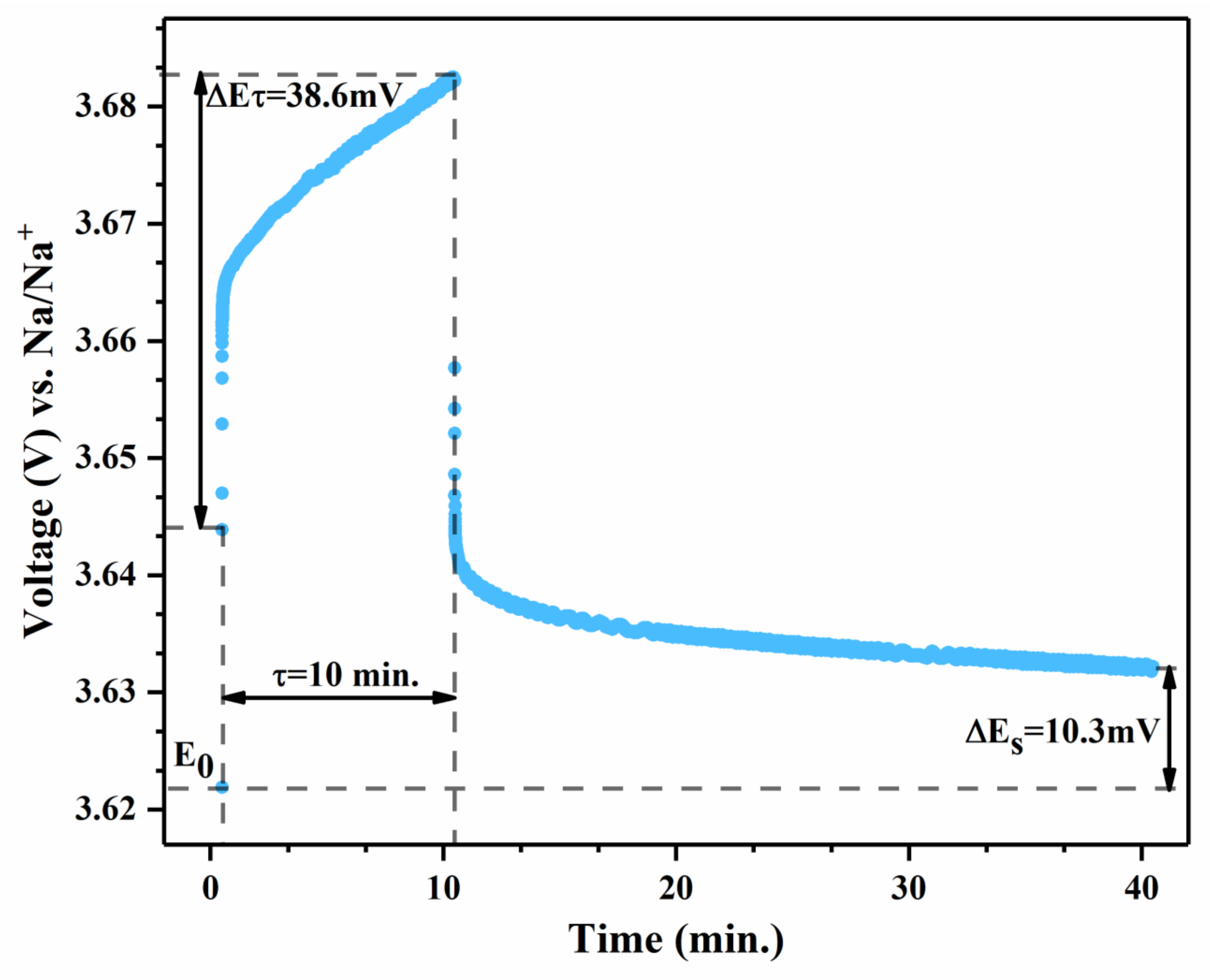

Figure S8: Illustration of the single titration unit of GITT during charging.

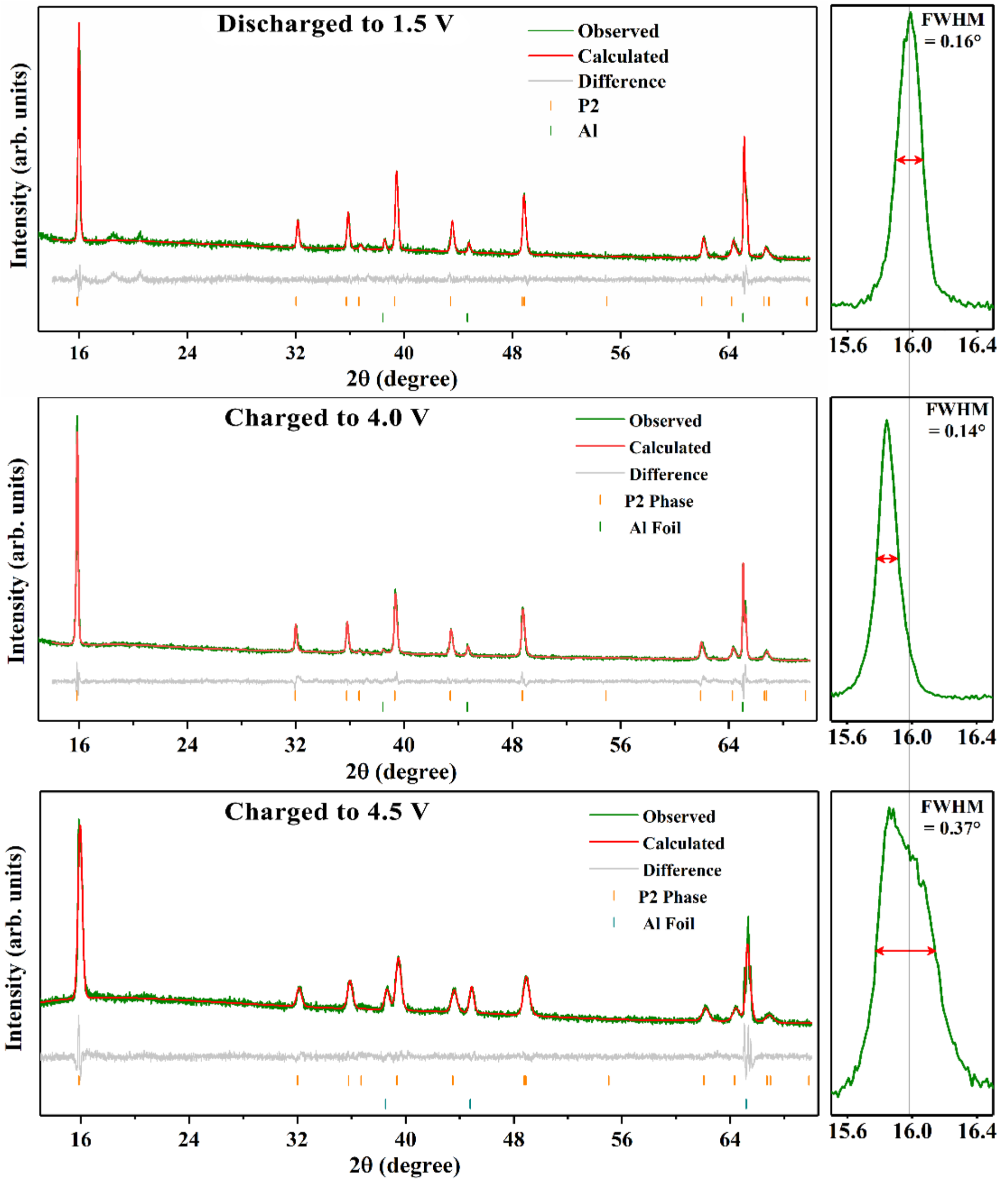

Figure S9: Ex-situ XRD patterns, along with fitted profiles, for the NMNT cathode at various states of charge (1.5 V, 4.0 V, and 4.5 V).

Table S1: Results of Rietveld refinement of room temperature powder x-ray diffraction data for NMN. *x*, *y*, *z* — positional coordinates. Reliability Factors: R_{EXP}, R_{WP}, R_P, and GoF were 7.49, 12.15, 8.71, and 1.62, respectively.

Atom	N_p	*x*	*y*	*z*	*Occupancy*
Na1	2	0	0	0.25	0.22
Na2	2	0.667	0.333	0.25	0.45
Mn/Ni	2	0	0	0	0.667/0.333
O	4	0.667	0.3333.	0.0934(6)	1

Table S2: Results of Rietveld refinement of room temperature powder x-ray diffraction data for NMNT. *x*, *y*, *z* — positional coordinates. Reliability Factors: R_{EXP}, R_{WP}, R_P, and GoF were 2.70, 3.36, 2.58, and 1.24, respectively.

Atom	N_p	*x*	*y*	*z*	*Occupancy*
Na1	2	0	0	0.25	0.22
Na2	2	0.667	0.333	0.25	0.45
Mn/Ni/Ti	2	0	0	0	0.567/0.333/0.100
O	4	0.667	0.333	0.088(3)	1

Table S3: Atomic % of various constituent elements in NMN and NMNT as estimated by EDS measurements.

Elements	**NMN**	**NMNT**
Na	38.7	39.2
Mn	41.0	34.8
Ni	20.3	20.0
Ti	--	6.0

Table S4: Comparison of specific capacity and cyclability for various Ti-doped layered oxides for sodium-ion batteries.

Phase-Composition	**Voltage Range vs. Na^+/Na**	**Capacity (0.1C, $mAh\ g^{-1}$)**	**Capacity retention, cycles**	**Ref.**
P2-$Na_{0.67}Ni_{0.33}Mn_{0.37}Ti_{0.3}O_2$	2.0-4.3 V	92	72%, 200 (1C)	[1]
P2/O3-$Na_{0.85}Ni_{0.34}Mn_{0.33}Ti_{0.33}O_2$	2.2-4.4 V	116.7	80%, 200 (1C)	[2]
O3-$Na[Ni_{0.5}Co_{0.2}Mn_{0.3}]_{0.7}Ti_{0.3}O_2$	2.0-4.3 V	105.8	47%, 300 (1C)	[3]
O3-$NaNi_{0.45}Mg_{0.05}Mn_{0.4}Ti_{0.1}O_2$	2.0-4.0 V	124.2	82%, 200 (1C)	[4]
P2-$Na_{0.67}Ni_{0.33}Mn_{0.37}Ti_{0.3}O_{1.9}F_{0.1}$	2.0-4.4 V	140.3	77%, 300 (2C)	[5]
O3-$NaCu_{0.1}Ni_{0.3}Fe_{0.2}Mn_{0.2}Ti_{0.2}O_2$	2.0-3.9 V	130	87%, 100 (0.1C)	[6]
O3-$Na_{0.83}Li_{0.1}Ni_{0.25}Co_{0.2}Mn_{0.15}Ti_{0.15}Sn_{0.15}O_{2-\delta}$	2.0-4.2 V	108.6	89%, 100 (0.5C)	[7]
P2-$Na_{0.67}Ni_{0.33}Mn_{0.57}Ti_{0.1}O_2$	2.0-4.0 V	90	89%, 100 (1C)	**This work**
P2-$Na_{0.67}Ni_{0.33}Mn_{0.57}Ti_{0.1}O_2$	2.0-4.5 V	140	71%, 100 (0.1C)	**This work**
P2-$Na_{0.67}Ni_{0.33}Mn_{0.57}Ti_{0.1}O_2$	1.5-4.0 V	149	80%, 100 (0.33C)	**This work**

Table S5: Values of various circuit elements calculated from the equivalent circuit fitting of room temperature fitting data.

Parameter		**NMN**	**NMNT**
R_E (Ω)		5.3 ± 0.1	6.5 ± 0.2
R_{IL} (Ω)		191 ± 2	207 ± 1
R_{CT} (Ω)		892 ± 2	386 ± 2
R_{Total}		1088 ± 4	599 ± 3
CPE_{IL}	**Q_{IL} (s^n/ Ω)**	$(2.6 \pm 0.1) \times 10^{-5}$	$(2.23 \pm 0.05) \times 10^{-5}$
	n	0.744±0.004	0.765 ± 0.003
CPE_{CT}	**Q_{CT} (s^n/ Ω)**	$(11.41 \pm 0.04) \times 10^{-5}$	$(32.3 \pm 0.1) \times 10^{-5}$
	n	0.826 ± 0.001	0.752 ± 0.003
CPE_D	**Q_D (s^n/ Ω)**	$(3.61 \pm 0.04) \times 10^{-2}$	$(6.230 \pm 0.009) \times 10^{-3}$
	n	0.739 ± 0.004	0.7679 ± 0.0005

References:

[1] L. Wang, M.Y. Sun, L. Deng, Y.Q. Zheng, X.Y. Li, Y.S. Jiang, L. Zhao, Z.B. Wang, Ti^{4+} substitution suppressing P2-O2 phase transition to construct stable P2-$Na_{0.67}Ni_{0.33}Mn_{0.67}O_2$ cathode for long-term durable sodium-ion batteries, J. Energy Storage, 81 (2024) 110299.

[2] L. Yu, Z. Cheng, K. Xu, Y.X. Chang, Y.H. Feng, D. Si, M. Liu, P.F. Wang, S. Xu, Interlocking biphasic chemistry for high-voltage P2/O3 sodium layered oxide cathode, Energy Storage Mater., 50 (2022) 730-739.

[3] L. Tan, Q. Wu, Z. Liu, Q. Chen, H. Yi, Z. Zhao, L. Song, S. Zhong, X. Wu, L. Li, Ti-substituted O3-type layered oxide cathode material with high-voltage stability for sodium-ion batteries, J. Colloid Interface Sci., 622 (2022) 1037-1044.

[4] S. Zhao, Q. Shi, W. Feng, Y. Liu, X. Yang, X. Zou, X. Lu, Y. Zhao, Suppression of multistep phase transitions of O3-type cathode for sodium-ion batteries, Chin. Chem. Lett., 35 (2024) 108606.

[5] P. Zhou, J. Zhang, Z. Che, Z. Quan, J. Duan, X. Wu, J. Weng, J. Zhao, J. Zhou, Insights into the enhanced structure stability and electrochemical performance of Ti^{4+}/F^{-} co-doped P2-$Na_{0.67}Ni_{0.33}Mn_{0.67}O_2$ cathodes for sodium ion batteries at high voltage, J. Energy Chem., 67 (2022) 655-662.

[6] C.-C. Lin, H.-Y. Liu, J.-W. Kang, C.-C. Yang, C.-H. Li, H.-Y.T. Chen, S.-C. Huang, C.-S. Ni, Y.-C. Chuang, B.-H. Chen, C.-K. Chang, H.-Y. Chen, In-situ X-ray studies of high-entropy layered oxide cathode for sodium-ion batteries, Energy Storage Mater., 51 (2022) 159-171.

[7] H. Wang, X. Gao, S. Zhang, Y. Mei, L. Ni, J. Gao, H. Liu, N. Hong, B. Zhang, F. Zhu, W. Deng, G. Zou, H. Hou, X.-Y. Cao, H. Chen, X. Ji, High-Entropy Na-Deficient Layered Oxides for Sodium-Ion Batteries, ACS Nano, 17 (2023) 12530-12543.